ELSEVIER

Contents lists available at ScienceDirect

Science of the Total Environment

journal homepage: www.elsevier.com/locate/scitotenv





Characterization of the aerosol vertical distributions and their impacts on warm clouds based on multi-year ARM observations

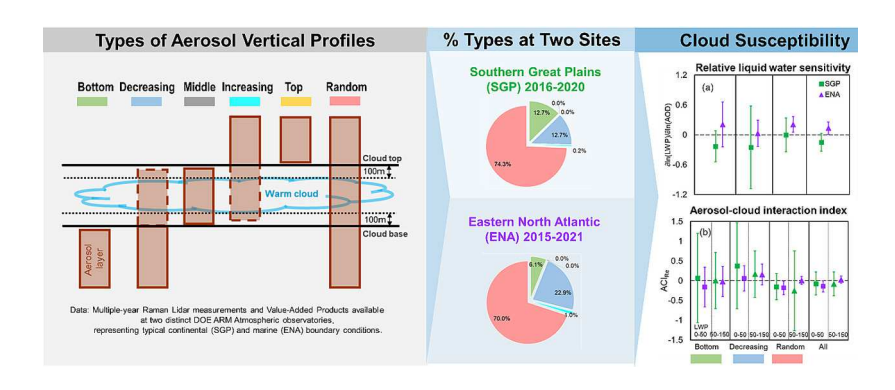
Yun Lin^{a,*,1}, Yoshihide Takano^{a,1}, Yu Gu^a, Yuan Wang^b, Shujun Zhou^a, Tianhao Zhang^a, Kuilin Zhu^a, Jingyu Wang^c, Bin Zhao^d, Gang Chen^a, Damao Zhang^d, Rong Fu^a, John Seinfeld^e

- ^a Department of Atmospheric and Oceanic Sciences, Joint Institute for Regional Earth System Science and Engineering, University of California, Los Angeles, CA 90095, United States
- ^b Department of Earth System Science, Stanford University, Stanford, CA, United States
- ^c National Institute of Education, Nanyang Technological University, Singapore
- d Atmospheric Sciences and Global Change Division, Pacific Northwest National Laboratory, Richland, WA 99352, United States
- e California Institute of Technology, Pasadena, CA 91125, United States

HIGHLIGHTS

- Upper-level AOD at SGP peaks in summer and early evening.
- A bimodal seasonal distribution is observed at ENA for lower-level AOD.
- Random, Decreasing, and Bottom are the primary vertical distributions at both sites.
- Aerosols tend to suppress cloud water production at SGP but invigorate it at ENA.
- AOD-droplet effective radius relations vary with aerosol vertical distributions.

GRAPHICAL ABSTRACT



ARTICLE INFO

Editor: Anastasia Paschalidou

Keywords:
Aerosol-cloud interactions
Aerosol vertical distribution types
Cloud microphysics
Raman Lidar
Continental-marine contrast

ABSTRACT

Aerosol vertical distribution plays a crucial role in cloud development and thus precipitation since both aerosol indirect and semi-direct effects significantly depend on the relative position of aerosol layer in reference to cloud, but its precise influence on cloud remains unclear. In this study, we integrated multi-year Raman Lidar measurements of aerosol vertical profiles from the U.S. Department of Energy Atmospheric Radiation Measurement (ARM) facility with available Value-Added Products of cloud features to characterize aerosol vertical distributions and their impacts on warm clouds over the continental and marine ARM atmospheric observatories, i.e., Southern Great Plains (SGP) and Eastern North Atlantic (ENA). A unimodal seasonal distribution of aerosol optical depths (AODs) with a peak in summer is found at upper boundary layer over SGP, while a bimodal distribution is observed at ENA for the AODs at lower levels with a major winter-spring maximum. The diurnal mean of upper-level AOD at SGP shows a maximum in the early evening. According to the relative positions of aerosol layers to clouds we further identify three primary types of aerosol vertical distribution, including

^{*} Corresponding author.

E-mail address: yunlin@ucla.edu (Y. Lin).

¹ Yun Lin and Yoshihide Takano: these authors contributed equally to this work.

Random, Decreasing, and Bottom. It is found that the impacts of aerosols on cloud may or may not vary with aerosol vertical distribution depending on environmental conditions, as reflected by the wide variations of the relations between AOD and cloud properties. For example, as AOD increases, the liquid water paths (LWPs) tend to be reduced at SGP but enhanced at ENA. The relations of cloud droplet effective radius with AOD largely depend on aerosol vertical distributions, particularly showing positive values in the Random type under low-LWP condition (<50 g m $^{-2}$). The distinct features of aerosol-cloud interactions in relation to aerosol vertical distribution are likely attributed to the continental-marine contrast in thermodynamic environments and aerosol conditions between SGP and ENA.

1. Introduction

Aerosols are one of the most critical climate-forcing agents, significantly contributing to the overall uncertainties in human-induced global radiative forcing estimation (Boucher et al., 2013; Kahn, 2012). Factors contributing to the uncertainties in aerosol radiative forcing include properties (Chen et al., 2023; Gu et al., 2016) and spatiotemporal variations (Chen et al., 2022; Kokhanovsky et al., 2010; Li et al., 2009) of aerosol and clouds, aerosol-cloud interaction processes (Rosenfeld et al., 2014; Tao et al., 2012), intricate aerosol-cloud-climate feedback mechanisms (Boucher et al., 2013; Carslaw et al., 2010; Raes et al., 2010), thermodynamic conditions governing cloud responses to the presence of aerosols (Chen et al., 2014), and meteorological conditions determining the spatial and temporal distribution of aerosols (Huige et al., 2021; Whiteaker et al., 2002). Amidst all these factors, the vertical distribution of aerosols contributes the largest share of uncertainties (Johnson et al., 2004), e.g., the global aerosol direct radiative forcing uncertainties have been estimated to be around 1.0 W m⁻² (Myhre and Shindell, 2013), while aerosol vertical profile alone can contribute as much as 0.5 W m^{-2} (Chung et al., 2005).

The importance of the vertical distribution of aerosols in aerosol radiative effect and the radiative heating/cooling associated with largescale atmospheric dynamics has been highlighted in a number of studies (Chand et al., 2009; Peters et al., 2011; Zarzycki and Bond, 2010). Aerosol vertical distributions substantially affect atmospheric radiative heating profiles (Léon, 2002; Won et al., 2004; Johnson et al., 2008; Zhang et al., 2013; Lin et al., 2022a) and modify atmospheric stability (Johnson et al., 2008; Mcfarguhar and Wang, 2006; Ramanathan et al., 2007), with potential changes in cloud properties (Johnson et al., 2004; Wang et al., 2020). They also influence the radiative effect at the top of the atmosphere (TOA), particularly when the aerosols have strong absorption of solar radiation (Gadhavi and Jayaraman, 2006; Johnson et al., 2008; Meloni et al., 2005; Zhang et al., 2013). The relative magnitude and even the sign of the aerosol effects are strongly affected by vertical distributions, especially the altitude concerning cloud layers. Wang et al. (2013) hypothesized that aerosol heating near the top of the planetary boundary layer (PBL) could stabilize the PBL increasing convection inhibition (CIN) within the PBL but enhancing convective available potential energy (CAPE) above the PBL. Over a longer timescale, suppressing shallow convection due to absorbing aerosols can postpone the release of energy and moisture, thus later feeding and enhancing deep convection (Fan et al., 2015; Wang et al., 2018). Instead of delayed formation of clouds by dust above clouds, Zhao et al. (2022) found that dust aerosols near surface tend to cause the early formation of clouds. In addition, Sun and Zhao (2020, 2021) revealed that the change of atmospheric vertical thermal structure (atmospheric stability) and precipitation initiation time are also dependent on the aerosol vertical distribution.

Understanding aerosol variability as a function of height is also important for aerosol-cloud interaction (ACI) because aerosol indirect (or microphysical) effects, by serving as cloud condensation nuclei (CCN) and ice nucleating particles (INPs), primarily depend on the aerosols that mix and interact with clouds (e.g., Zhao et al., 2018a; Lin et al., 2022b). There is increasing evidence that aerosols can alter cloud microphysical properties and enhance the indirect effect via

entrainment into the cloud top from the plume above (Lu et al., 2018; Painemal et al., 2014). Based on satellite observations, Costantino and Bréon (2013) found that the dry effect due to aerosol enhanced entrainment of dry air at the cloud top competes with the moistening effect due to aerosol inhibition of precipitation and yields a decrease in liquid water path (LWP) for warm clouds over the South-East Atlantic. The degree of aerosol effects on cloud microphysics also depends on the vertical distribution of aerosols (Diamond et al., 2018; Wang et al., 2020). The idealized modeling study by Zhang et al. (2021) suggests that only the initial aerosol layer at the comparable altitude to the cloud layer or with aerosols distributed in all the levels within lower boundary layer (e.g., 0-5 km) can allow aerosols to efficiently enter cloud and provide an effect on deep convective cloud microphysics and precipitation. Aerosol semi-direct effects that are related to aerosol radiative effects, on the other hand, are mainly dependent on the relative position of aerosol layers to clouds (Gu et al., 2010; Gu et al., 2016; Hansen et al., 1997; Johnson et al., 2004). Herbert et al. (2020) revealed that the daily mean semi-direct effect can be significantly altered by the distance between cloud and absorbing aerosol layer, aerosol layer thickness, and aerosol number density.

Characterization of aerosol profile parameters, particularly from an observational perspective, can therefore increase the accuracy in modeling the vertical distributions of aerosols and estimating aerosol impacts on radiative forcing and cloud formation (Haywood and Boucher, 2000; Kaufman et al., 2002; Ramanathan et al., 2001). The vertical distributions of aerosols are affected by a number of atmospheric processes, including emission, transport, deposition, as well as microphysical and chemical processes, which are dynamically changed at different vertical levels. These complex atmospheric processes cannot be fully considered in the current modeling approach, which therefore results in considerable uncertainties. Various assumptions on aerosol vertical distributions have been used in previous retrieval studies. For example, the Gaussian distribution was applied in the algorithms of the Deep Blue aerosol optical depth (AOD) (Hsu et al., 2004), the retrieval of the layer height for typical smoke (Lee et al., 2015), and the aerosol retrieval of Polarization and Directionality of the Earth's Reflectance (POLDER) (Dubovik et al., 2011b), while the exponential distribution was applied to all aerosol models in the MODIS Dart Target AOD algorithm over land (Levy et al., 2007).

A number of field programs have been carried out to measure the vertical distributions of aerosols, including the Dust and Biomassburning Experiment (DABEX), Tropospheric Aerosol Radiative Forcing Observation Experiment (TARFOX), and Puerto Rico Dust Experiment (PRIDE) (Huebert et al., 1998; Johnson et al., 2008; Maring, 2003; Russell et al., 1999). These ground-based and/or aircraft measurements have provided valuable information, but are limited in spatial and temporal coverage, particularly unable to characterize the diurnal variation and seasonality of aerosol profile patterns. Satellite observations, such as the Cloud-Aerosol Lidar with Orthogonal Polarization (CALIOP) on board the Cloud-Aerosol Lidar and Infrared Pathfinder Satellite Observation (CALIPSO), have continuously conducted observations of the global atmospheric aerosol vertical distributions since 2006 (Winker et al., 2009). However, the satellite products suffer bias because of cloud contamination or surface contamination in AOD retrieval (Kaufman et al., 2005; Kim et al., 2017). CALIPSO is especially

subject to issues like surface contamination when detecting aerosols at altitude below 200 m a.g.l. and missing detecting optically thin aerosol layers at higher levels due to insufficient detection sensitivity (Thorsen et al., 2017).

The long-term, high-temporal-resolution measurements from various lidar systems operated by U.S. Department of Energy (DOE) Atmospheric Radiation Measurement (ARM) facility provide unique datasets of aerosol vertical profile and cloud information and enable a comprehensive analysis of the characteristics of aerosol vertical distributions and their impacts on cloud properties (Ackerman and Stokes, 2003; Schmid et al., 2006; Schmid et al., 2009). These measurements have provided a large number of samples across a wide variety of meteorological conditions, which, compared to orbital satellite data, can better help understand the temporal variations of aerosol vertical distributions and assess how these different distributions influence cloud development and properties. In addition, the lidar measurements-based analysis can serve as a benchmark to verify the results based on other airborne data.

In this study, we primarily employed the multi-year Raman Lidar (RL) observations and retrievals of vertical information of aerosols and clouds, as well as other measurements relating to cloud properties at two ARM atmospheric observatories, namely, Southern Great Plains (SGP) and Eastern North Atlantic (ENA), to characterize aerosol vertical distribution and investigate its possible effects on aerosol-warm cloud interactions under different boundary layer conditions. The aerosol vertical distribution patterns and their temporal variability were examined over the two sites. The responses of cloud macro- and microphysical parameters to aerosol loadings were examined with respect to aerosol vertical distribution types, and the significance of the difference in aerosol-cloud interactions between continental and marine conditions were highlighted through the comparison between the SGP and ENA sites. AOD was taken as the proxy of aerosol loadings in this study.

2. Data and methods

2.1. ARM measurements

The DOE ARM Climate Research Facility (ACRF) has deployed various lidar systems at each site, providing long-term continuous observations of aerosol profiles with high vertical and temporal resolutions (Ackerman and Stokes, 2003; Mather and Voyles, 2013). The RL measurements used in this study can separate molecular and particulate signals and provide aerosol backscatter and extinction coefficient vertical profiles by using return signals from elastic backscatter at 355 nm and Raman-shifted backscatter due to atmospheric nitrogen at 387 nm (Chand et al., 2019). Thorsen et al. (2015) used three scattering ratios from ARM RL elastic and nitrogen channel signals, as well as the total volume depolarization ratio at the elastic channel, to detect atmospheric features if derived scattering ratio and depolarization ratio are larger than range-dependent detection thresholds. The detected atmospheric feature is further classified as aerosol, liquid cloud, or ice cloud using the relation between lidar depolarization and particulate backscattering coefficient thresholds (Thorsen and Fu, 2015). One advantage of using RL measurements over satellite retrievals is that RL does not have the issue of missing detection of optically thin aerosol layers, which has been found in CALIPSO observations frequently due to its insufficient detection sensitivity (Thorsen et al., 2017).

We employed the ARM Raman Lidar Profiles-Feature detection and Extinction (RLPROF-FEX) Value-Added Product (VAP) for aerosol layer structure detection, which implements the feature detection and classification algorithms to RL measurements (Chand et al., 2019). RLPROF-FEX is a product generated at a 2-min temporal frequency and 30-m vertical resolution with 667 altitude levels. Given that columnintegrated AOD is an important and widely used parameter to quantify aerosol impacts in current studies, we derived column AOD using the

RLPROF-FEX product by vertically integrating aerosol extinction coefficients with certain quality controls, i.e., total detection confidence score > 0.3 and missing and inadequate profile measurements excluded with 'qc_profile' equal to 1, 2, or 3 (Chand et al., 2019). The RL signal and extinction could be largely biased due to the lidar near-range overlap issue and thereby the extinction data at lower altitudes should be used with caution (Wang and Menenti, 2021), and we found that the bias is particularly significant for the lowest level of RL measurements (0-30 m). Therefore, the lowest layer was excluded for layer AODs calculation in this study. However, it should be noted that the exclusion of the lowest layer from our calculations may introduce a certain degree of underestimation in the estimation of integrated AOD. Previous studies also suggested that the AOD estimation likely exhibits significant enhancement bias in the vicinity of clouds due to contamination by undetected clouds, aerosol humidification, and meteorological conditions (Altaratz et al., 2013; Chand et al., 2012), and the enhancement can be as high as 25 % in cloudy conditions (Chand et al., 2012). Therefore, our analysis focused on clear-sky aerosol profiles with excluding those profiles that are five minutes close to cloud profile to avoid cloud contamination.

To comprehensively characterize aerosol vertical distribution, we also explored other aerosol parameters, such as aerosol layer geometric thickness, mean aerosol height, and aerosol scale height. These variables can describe the aerosol layer shape and altitude of a specific distribution like exponential or random/Gaussian distributions (Wu et al., 2017). These aerosol-related variables are also important factors in defining aerosol vertical distributions in retrieval algorithms (Dubovik et al., 2011a; Hsu et al., 2004; Lee et al., 2015; Levy et al., 2007) or climate models (e.g., Gu et al., 2006). In this study, aerosol scale height was determined as the altitude where the extinction coefficient decreases to 1/e of its surface level. Aerosol layer structures like aerosol layer top and base heights were identified based on the altitude information associated with 'aerosols' features masked in the RLPROF-FEX product, and then mean aerosol height and aerosol layer thickness were calculated by averaging the sum of aerosol layer top and base heights and contracting aerosol layer top height from its base heights, respectively. If a clear void exists in the aerosol layer, it was removed from the average.

Cloud macro- and microphysical properties were based on the synergy of multiple instruments and are available from various ARM VAPs. The Ka-band ARM Zenith Radar (KAZR) Active Remote Sensing of Clouds (KAZRARSCL) VAP provides reliable cloud boundary detections using best estimates from KAZR, Micropulse lidar-derived cloud mask, and ceilometer-derived lowest cloud base. In this study, we only focus on single-layer clouds to avoid the complexity of the clouds with multiple layers. Cloud top and base heights were derived from the detected cloud boundaries, and cloud geometric thickness is calculated as the distance between cloud top and base heights. Cloud LWP is available from the MWRRET VAP (https://www.arm.gov/capabilities/vaps /mwrret), which retrieves LWP from the measurements of microwave radiometer brightness temperature using the optimal estimation method developed by Turner et al. (2007). The layer-mean liquid water content (LWC) is obtained by dividing the LWP with cloud thickness assuming that LWP linearly increases with the distance above the clouds base. Note that the linear relationship between LWP and cloud thickness does not always hold considering the existence of entrainment around cloud tops and/or the collision-coalescence processes when drizzle exists (Zhao et al., 2012), which might lead to some bias in LWC calculation using the linear relationship assumption. Nevertheless, the LWC calculation employed in this study can represent the average status of cloud liquid water content in all cloud levels in a column. We used the RLPROF-FEX extinction coefficient (β_e) masked with "liquid cloud" feature to calculate cloud optical depth (COD) in the form

$$COD = \int_{z_b}^{z_t} \beta_e dz, \tag{1}$$

where z_t and z_b are the cloud top and base heights, respectively. The retrieval of COD was made only for RL transparent profiles, which are described as when the signals from RL pass completely through the atmosphere without being fully attenuated before reaching an altitude beyond clouds. With excluding non-transparent profiles, we were able to improve the accuracy of the aerosol-cloud interaction evaluations by ruling out the interferences from incomplete cloud profiles. Specifically, we defined transparent profiles with a signal-to-noise ratio (SNR) >1 at 16 and 18 km for SGP and ENA, respectively, similar as Balmes et al. (2019). Also, we inferred the layer mean cloud effective radius (R_e) following Han et al. (1995) as

$$R_{e} = \frac{3}{2\rho_{i}} LWP / COD, \tag{2}$$

where ρ_l (=1 g cm⁻³) is the density of water and the units of R_e and LWP are micrometer (μ m) and g m⁻², respectively.

The two ARM atmospheric observatories, i.e., SGP and ENA, were chosen for study because of their distinct aerosol sources and thermodynamic conditions, in addition to their availability of long-term observations and retrievals in aerosol and cloud. The SGP central facility site, located near Lamont, in north-central Oklahoma (36.61°N, 97.48°W), represents continental clouds and aerosols with episodes of pollution and biomass burning smoke from the Gulf of Mexico and Central America (Logan et al., 2018). The ENA atmospheric observatory, located on Graciosa Island in the Azores archipelago, Portugal (39.09°N, 28.03°W), is dominated by marine boundary layer clouds (e.g., shallow cumulus, stratocumulus, and stratus) which are present throughout the year due to semi-permanent high pressure systems (Rémillard et al., 2012), with periodic episodes of aerosols from North and Central America (pollution and biomass burning), Africa (Saharan dust), and the surrounding ocean (sea salt) (Logan et al., 2014; Osborne and Haywood, 2005). We employed the measurements during 2016–2020 at SGP and 2015–2021 at ENA for the following analysis in order to understand the different features of aerosol vertical distributions and aerosol-cloud interactions under different environmental conditions in which warm clouds form.

2.2. Aerosol-cloud collocation

To characterize vertical distributions of aerosols that may influence warm clouds, the aerosol measurements with cloud observations were first collocated following a similar method as Zhao et al. (2019). Based on the feature mask of RLPROF-FEX VAP, we checked a time frame one hour before the starting time of a certain cloud system passing the site and one hour after it to examine whether any clear-sky aerosol profiles, which are also five-minute away from the cloud, exist. If they exist, these cloud and aerosol profiles are adopted for further analysis. To reduce interference from mixed- and ice-phase clouds, only the single-layer clouds with cloud top temperatures warmer than 0 $^{\circ}\text{C}$ were selected for study. To reduce uncertainty, we only focused on cloud profiles with cloud thickness < 3 km and cloud duration time > 1 h to eliminate scuds or tiny clouds. Together with the selection of transparent profiles, it turns out that this study most likely focused on low-level optically-thin clouds. The cloud profile was ignored if there was no available aerosol observation within the 1-h time frame. All the clear-sky aerosol profiles sampled in the time frame were averaged to get the mean aerosol profile associated with one cloud profile. With the collocation of clouds with aerosol vertical profiles we find a total of 262 warm cloud cases associated with 409 effective aerosol vertical profiles at SGP during 2016-2020 and 564 warm cloud cases associated with 1053 effective aerosol vertical profiles at ENA during 2015-2021.

2.3. Covariation of meteorological factors

One possible interference of aerosol-cloud correlations stems from

the covariations of aerosol loadings and cloud properties with meteorological conditions. To evaluate this interference of covarying meteorological fields, we first assessed the extent to which the relations of cloud properties with AOD are similar under different meteorological regimes, following Zhao et al. (2018b). If the relationships between aerosol and cloud change greatly under different meteorological regimes, it suggests that the meteorological variables may play a role in modulating aerosol-cloud interactions. On the other hand, to isolate aerosol effect from the contribution of metrological covariations, we further binned cloud features according to meteorology parameters and examined the relations between cloud features and meteorology parameters under different ranges of AOD. If the responses of cloud features to a certain meteorology parameter are distinct under different AOD ranges at the given meteorological condition, we can attribute the alterations of cloud properties under different aerosol pollution condition to the aerosol effect.

The meteorological fields examined here include relative humidity (RH), lower tropospheric stability (LTS), vertical wind shear (VWS), temperature, vertical velocity (VV), and CAPE. To incorporate the most relevant meteorological variables possibly influencing the cloud formation and evolution, we focused on the mean meteorological conditions extracted at or averaged over warm cloud levels during cloud periods. For example, the mean RH and temperature were averaged over the layer of 750–850 hPa (i.e., RH_{750-850hPa} and T_{750-850hPa}), VWS was calculated between 725 and 925 hPa (VWS_{725-925hPa}), and the mean VV was averaged over 750–850 hPa (VV_{750-850hPa}). In addition, LTS was derived following Klein and Hartmann (1993) as the 700-hPa potential temperature minus the near-surface potential temperature (LTS_{700hPa}).

We used ARM radiosonde data (the INTERPSONDE VAP, https://www.arm.gov/capabilities/science-data-products/vaps/interpsond e) with interval of about 5 times a day for temperature, pressure, and RH. For air vertical velocity, we adopted Doppler lidar data with a temporal resolution of 10 min and a height resolution of 30 m. This and other meteorological data were interpolated linearly at the time-height grid of cloud and aerosol variables.

3. Results and discussion

3.1. Characteristics of aerosol vertical distribution

3.1.1. Seasonality and diurnal variations

The multi-year mean and standard deviation of column-integrated daily AOD at the SGP and ENA sites are 0.23 \pm 0.13 and 0.12 \pm 0.08, respectively. To detect the seasonal dependency of aerosol vertical distributions, the layer AODs were binned into various height ranges, i.e., 0-200 m, 200-500 m, 500-1000 m, 1000-1500 m, 1500-2500 m, and >2500 m a.g.l. for SGP and 0-200 m, 200-400 m, 400-600 m, 600-800 m, 800–1200 m, and >1200 m for ENA. Fig. 1 shows the seasonal variations of layer AOD and aerosol extinction coefficient as a function of height. In a striking pattern, the AOD seasonal variations are vastly different between the lower and upper altitudes at SGP (Fig. 1a). For example, the monthly mean AODs of the vertical layers below 1 km do not show a clear primary peak, while those above 1 km of ground level have maxima in summer. The integration of all vertical layer AODs thus results in a nearly unimodal distribution at SGP, with a peak in summer. In addition, it is found in Fig. 1c that aerosols in all the seasons except winter are well mixed at lower boundary layers (e.g., below 2 km in summer) and then exponentially decrease, while in winter they always decrease rapidly with altitude starting from ground. Consistently with the higher mixing layer, the aerosol layer top height (i.e., aerosol extinction $>\!\!0.001~\text{km}^{-1}\!)$ can reach 6 km in summer, which is about 3 km higher than in winter.

Similar seasonality of aerosol vertical distributions was reported over the Eastern United States (EUS) based on CALIPSO satellite observations (Huang et al., 2013; Zhao et al., 2018b). The summer peak of upper level AOD can be attributed to more frequent and efficient

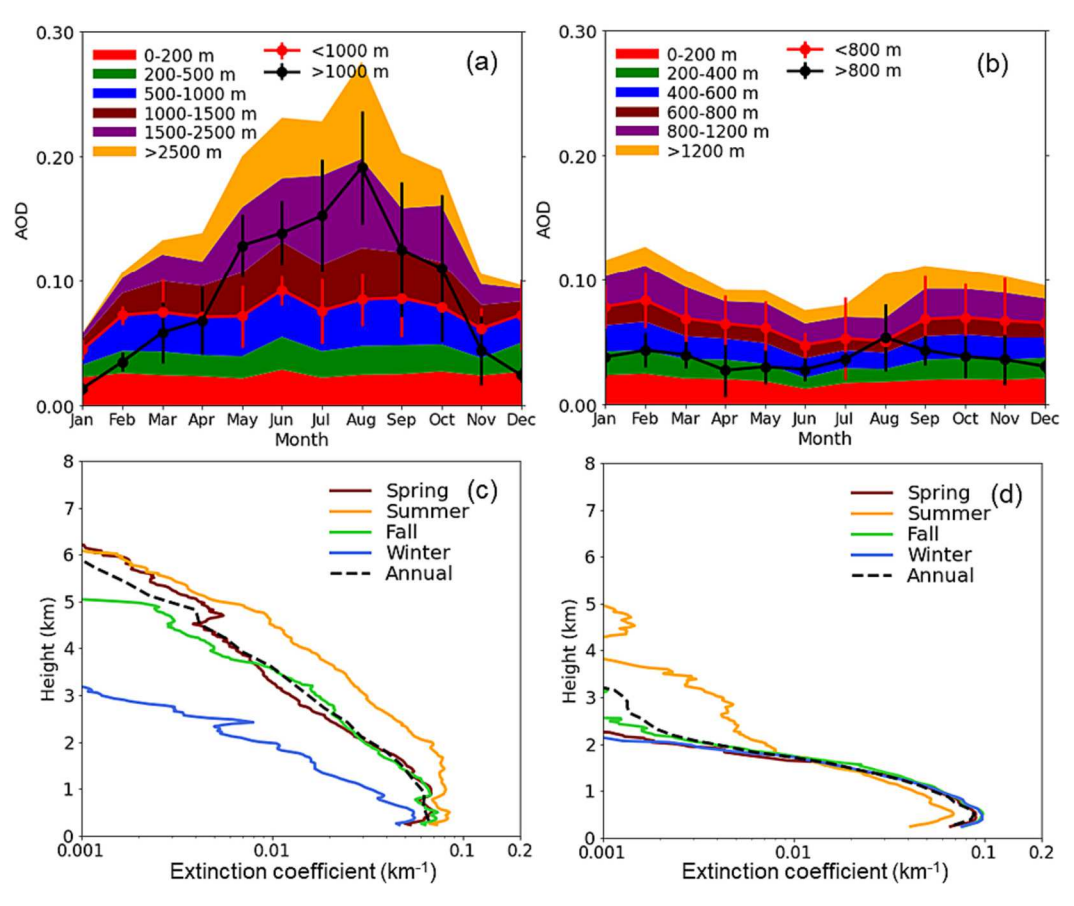


Fig. 1. Seasonal variations of layer AOD at (a) SGP and (b) ENA, and seasonal and annual mean extinction coefficient profiles at (c) SGP and (d) ENA. In panels (a) and (b), the range of AOD within a particular height range is depicted by the colored stacks. The integrated AODs for heights below (red) and above (black) 1000 m/800 m for SGP/ENA are shown as solid lines, for which the error bars are defined as the standard deviations of the monthly mean AOD values estimated over all the years. Both seasonal mean AOD and aerosol extinction vertical distributions were derived over cloud-free aerosol profiles measured at SGP during 2016–2020 and at ENA atmospheric observatories during 2015–2021.

transport of lower aerosols to upper levels, due to stronger vertical mixing in summer (Zhao et al., 2018b). In contrast, the aerosol mixing layer is confined to lower levels in winter due to generally stable atmosphere in this season. Another possible reason leading to more aerosols at upper levels in summer is related to intensive secondary organic formation at high levels because of warm temperature in summer (De Reus et al., 2000; Minguillón et al., 2015; Zhao et al., 2018b). Huang et al. (2013) noted that transport of polluted dust and smoke at elevated levels prevail in summer over the EUS region, which could also result in the summer AOD peak at upper levels observed over SGP. The transitional seasons of spring and fall are in between summer and winter; however, spring has apparent higher aerosol loadings above 3.5 km than fall. This results from the fact that the majority of the troposphere responds more slowly to changes in solar radiation than the ground (and lowest part of the troposphere). In spring, the near-ground part of the atmosphere warms quickly but the rest of it remains rather cold from winter, so that instability is greater. In fall, the low-levels cool more quickly while the remainder stays rather warm from the leftover effects of summer.

At ENA, the column-integrated AOD over all vertical layers shows a bimodal seasonal distribution, with a major peak in late winter and a minor peak in fall. A similar distribution has also been reported in Cimel and MODIS observations at ENA by Wood et al. (2015), albeit with the major peak occurring in early spring, somewhat later than that observed in this study. The winter-spring AOD peak can be attributed to continental pollution transported from North America, which is due to strong zonal westerlies and lofting of pollutants by cold fronts (Liang et al., 2004; Zhao et al., 2012). Since there is also an AOD spike of the vertical

layers above 800 m in summer, it seems that the bimodal pattern is controlled by the AOD seasonality of the vertical layers both below and above 800 m (Fig. 1b). The difference in seasonal AODs between lower and upper heights at ENA is also evident in the seasonal mean aerosol extinction vertical profiles (Fig. 1d), showing that the aerosol extinction in summer is smaller below 1.5 km than other seasons but higher above 1.5 km. The aerosol layer top height is about 4 km in summer, higher than other seasons by 2–2.5 km (Fig. 1d). The higher aerosol layer top with lower tropospheric aerosol abundance in summer has been observed over the North Atlantic Ocean based on satellite observations (Huang et al., 2013). Compared to SGP, most aerosols observed at ENA are confined below 2 km with a mean scale height of about 650 m, while the aerosol layer at SGP can extend as high as 5 km with a mean aerosol scale height of 1.5 km. Overall, the seasonal variations of column AOD and aerosol vertical distributions at ENA are less significant than at SGP.

The column AOD at SGP also shows clear diurnal variation. The mean daily maximum and minimum AODs are about 0.18 and 0.13 at around 18:00 LT and 3:00 LT, respectively, and the relative daily range of AOD is about 40 %. The diurnal cycle of column AOD at SGP is induced mainly by the diurnal variation of AODs of the vertical layers above 1000 m (black line in Fig. 2a), while the AODs of the vertical layers below 1000 m barely change with time (red line in Fig. 2a). The mean aerosol extinction profile at 18:00 LT shows that aerosols mix well below 2 km and then exponentially decrease ascending above 2 km (Fig. 2c). In contrast, the mean aerosol extinction profile at 03:00 LT displays an exponential decreasing pattern starting from near ground. There is no evident diurnal cycle at ENA (Fig. 2b), with the relative range of diurnal variation <20 %. Consistently, the vertical distribution

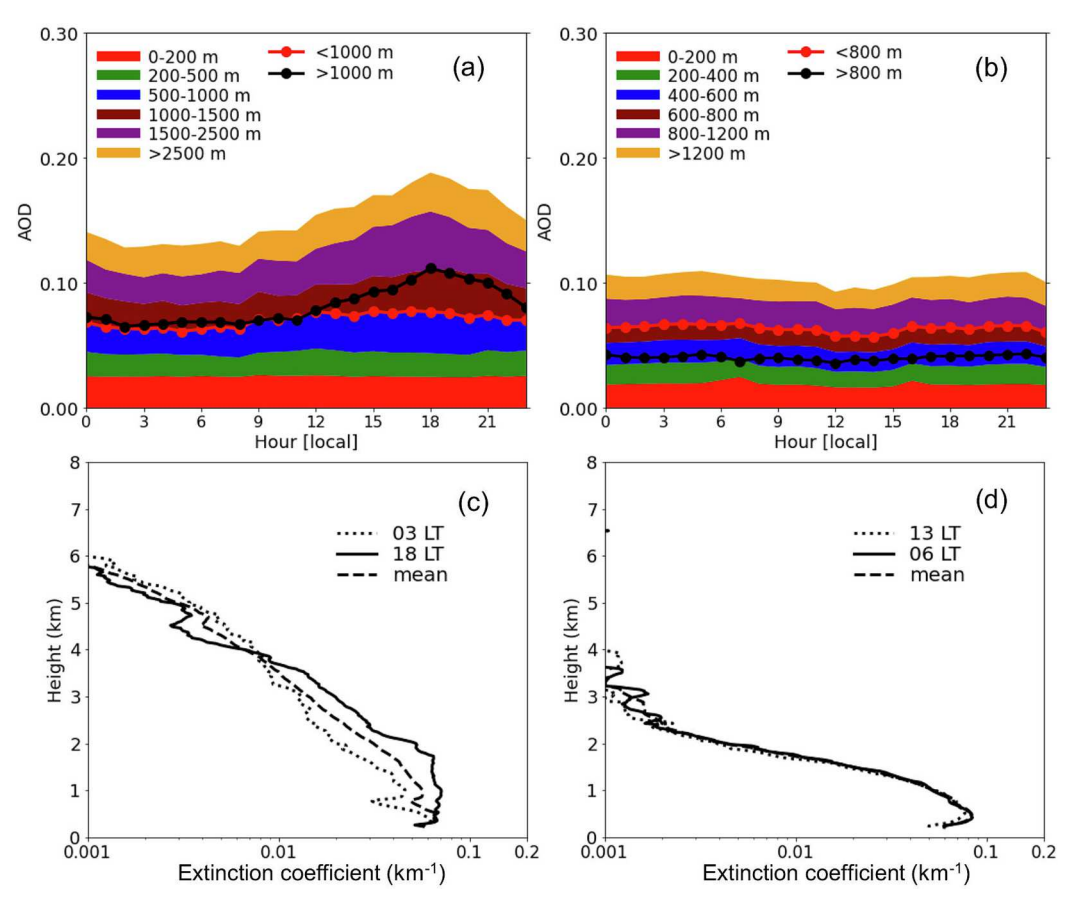


Fig. 2. Diurnal variations of layer AOD at (a) SGP and (b) ENA, and daily mean extinction coefficient profiles (dashed lines) and extinction coefficient profiles at hours with minimal (dotted lines) and maximal (solid lines) column AOD at (c) SGP and (d) ENA. In panels (a) and (b), the range of AOD within a particular height range is depicted by the colored stacks. The integrated AODs for heights below (red) and above (black) 1000/800 m for SGP/ENA are shown as solid lines.

pattern of aerosol extinction is quite similar at different hours, all showing a Gaussian distribution (Fig. 2d). The distinct characteristics of aerosol vertical distribution and its seasonal and diurnal variations observed at the two ARM sites may lend support to the necessity of classifying aerosol vertical types when collocating aerosol-cloud cases and evaluating aerosol-cloud interactions.

3.1.2. Classification with respect to cloud layer

With the collocation of clouds with aerosol vertical profiles, it is

found that the aerosol vertical position relative to the cloud layer shows a large diversity at SGP (Fig. 3a), i.e., the mean height of aerosol layers can be either lower or higher than or comparable to that of cloud layers. At ENA the cloud layers occurring above 1 km are generally higher than aerosol layers, but there are still considerable cases below 1 km with cloud layer height comparable to or even lower than aerosol layers (Fig. 3b). These large variations of aerosol-cloud relative position can lead to different mechanisms for aerosols entering clouds, e.g., pumping from cloud base or entrainment from cloud top with cloud vertical

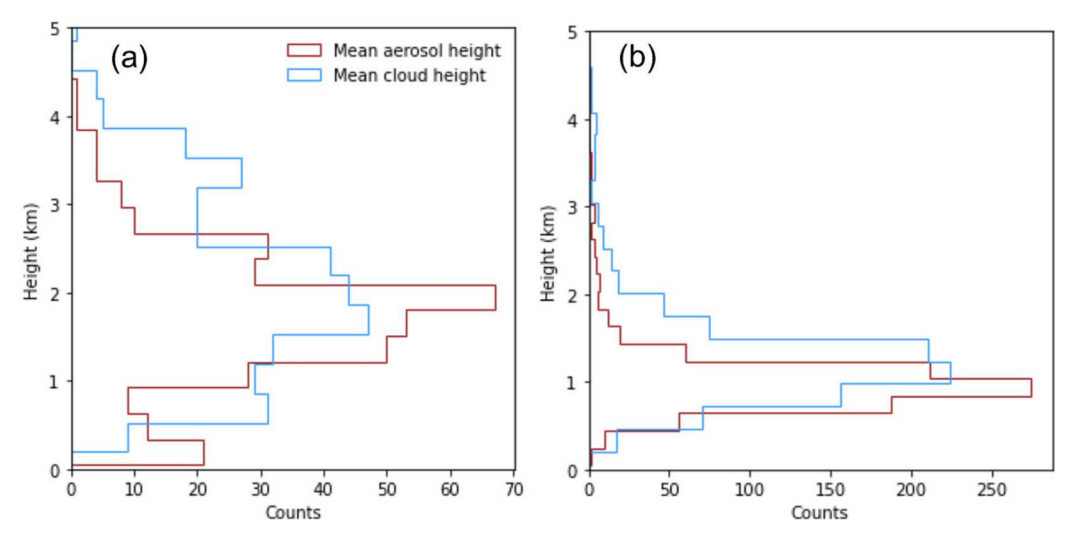


Fig. 3. PDF of aerosol and cloud layer mean heights at (a) SGP and (b) ENA.

development, eventually resulting in distinct CCN effects (Zhang et al., 2021). As such, it is worth classifying aerosol vertical distributions according to the relative position of aerosol layers to cloud layers.

When doing classification, the gap distance from cloud layer top to aerosol layer base was set as 100 m, i.e., the cloud top height was extended upward by extra 100 m to get a new cloud top boundary for comparison with aerosol layer height. This follows Costantino and Bréon (2013), in which they assumed that aerosols within this 100-m range above cloud layer can still physically interact with clouds. We applied the same gap distance value to extend the cloud base height downward, considering that aerosols below cloud are able to enter clouds through the pumping process as clouds develop and then make effects on cloud microphysical processes.

Six aerosol vertical types were predefined for classification, including Bottom, Decreasing, Middle, Increasing, Top and Random (Fig. 4a). The Bottom type refers to the aerosol-cloud collocated cases in which aerosol layers mainly exist near the surface and below the cloud level. As such, the cases with aerosol layer top height lower than the base height of the corresponding cloud were identified as this type. The Decreasing type is defined as the vertical distribution with more aerosols in the lower boundary layer and less in the upper layer, which is similar to the exponential or power-law functions used in aerosol retrieval algorithms (Wu et al., 2017). Specifically, the aerosol layer top in this type falls in the range from the corresponding cloud base to the cloud top, with the aerosol layer base lower than the cloud base. The Middle and Top types, in which aerosol layers mainly exist around and above the cloud level, respectively, represent the situations with long-range and/ or medium-range transported aerosols. The Middle type includes the cases with the aerosol top lower than the cloud top and the aerosol base higher than the cloud base, and the Top type includes the cases with the aerosol base higher than the cloud top. The Increasing type is characterized by more aerosols in the upper layer and less in the lower layer, which would cover the cases with the aerosol base higher than the cloud base but lower than cloud top and with the aerosol top always higher than the cloud top. In the Random type, aerosols are randomly distributed in the tropospheric column, and thus the cloud layer is normally embedded in the aerosol layer.

With the classification, three primary aerosol vertical distribution types are identified as Random, Decreasing, and Bottom at both sites, accounting for 74.3 %, 12.7 %, and 12.7 % of total cases over SGP, respectively, and 70.0 %, 22.9 %, and 6.1 % of total cases over ENA, respectively (Fig. 4b and c). The Increasing type shares only 0.2 % and 1.0 % of total cases at SGP and ENA, respectively, and no cases were recognized as the Top and Middle types at both sites. For the cases with long- and medium-range transported aerosols above cloud, appreciable aerosols are normally found below the cloud as well. These aerosols are anthropogenically originated from the ground and then mixed upward with aerosols from long- and medium-range transport. In addition, these low-level aerosols may be pumped into clouds and then participate in cloud development. Such cases are recognized as the Random type in this study because aerosols are present in all altitude levels, including cloud layer level. Therefore, the Random type is found as the most prevalent situation and there are limited or none samples categorized as Increasing, Middle or Top types. As such, the analysis in following sections will only focus on the three primary vertical types (i.e., Random, Decreasing, and Bottom).

The statistics of feature parameters of aerosol vertical distribution and aerosol loading are summarized in Table 1. In general, the aerosol layers in the Random type are highest and thickest, followed by the Decreasing and Bottom types. For example, the mean aerosol heights for Random, Decreasing, and Bottom are 1970, 1420, and 550 m, with corresponding mean aerosol layer thicknesses of 3310, 2630, and 840 m, respectively. Because of the thicker aerosol layer, the aerosol concentration is normally smaller (e.g., Boyouk et al., 2010, Ding et al., 2016, Li et al., 2017, etc.), resulting in a smaller aerosol extinction coefficient in the Random type than other types. The dependency of columnintegrated AOD on aerosol vertical type, on the other hand, varies with geolocation. For instance, the AODs are comparable in all the three

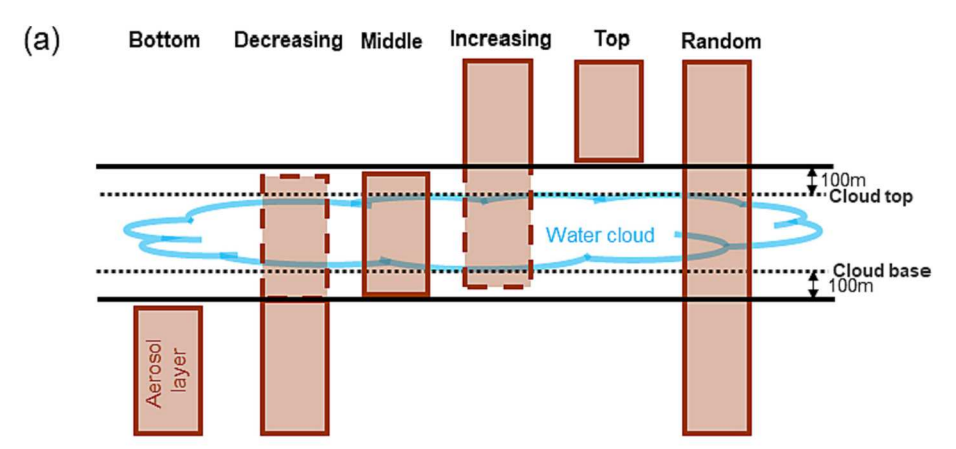


Fig. 4. (a) The schematic diagram of the six types of aerosol vertical distribution relative to cloud layer for aerosol-cloud collocation, including Bottom. Decreasing, Middle, Increasing, Top, and Random; the percentages of sample size in each aerosol vertical type identified at (b) SGP during 2016-2020 and (c) ENA site during 2015-2021. Brown boxes in (a) denote aerosol layer boundaries and the dashed sections of the boxes in Decreasing and Increasing types represent that the aerosol layer top height in Decreasing and the aerosol layer base height in Increasing vary between the corresponding cloud base and top heights. n values in parenthesis in (b) and (c) denote the total sample number at each site.

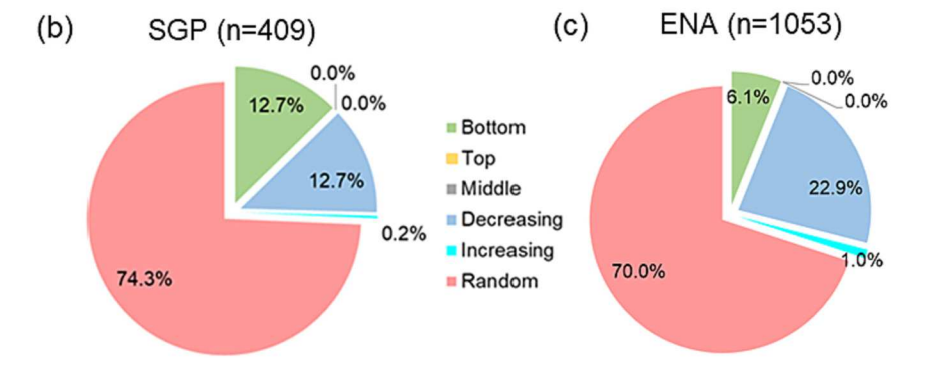


Table 1 Statistics (mean \pm σ) of feature parameters of aerosol vertical distribution, including mean aerosol height (μ), aerosol scale height (H), aerosol layer thickness (ΔZ), aerosol extinction coefficient (Ext), and column AOD, for different aerosol vertical types at SGP and ENA.

| Vertical types | μ (m) | H (m) | ΔZ (m) | Ext (km ⁻¹) | AOD |
|-------------------|-------------|------------|---------------|----------------------------|-------------|
| SGP | | | | | |
| Bottom | 550 \pm | 420 \pm | 840 ± 960 | 0.37 \pm | $0.19\ \pm$ |
| | 490 | 480 | | 0.36 | 0.16 |
| Decreasing | $1420\ \pm$ | 1310 \pm | $2630~\pm$ | 0.22 \pm | 0.42 \pm |
| | 490 | 620 | 1010 | 0.35 | 0.24 |
| Random | 1970 \pm | _ | $3310 \; \pm$ | 0.14 \pm | 0.42 \pm |
| | 630 | | 1180 | 0.10 | 0.27 |
| | | | | | |
| ENA | | | | | |
| Bottom | $800 \pm$ | 703 \pm | $1446 \pm$ | $0.11~\pm$ | $0.15 \pm$ |
| | 257 | 285 | 511 | 0.07 | 0.07 |
| Decreasing | 792 \pm | 747 \pm | $1423~\pm$ | 0.10 \pm | 0.14 \pm |
| | 220 | 285 | 452 | 0.04 | 0.06 |
| Random | $1123~\pm$ | _ | 1937 \pm | $0.09 \pm$ | 0.17 \pm |
| | 466 | | 677 | 0.04 | 0.08 |

types at ENA, with values falling in a narrow range of 0.14–0.17; in contrast, the AODs at SGP in the Random and Decreasing types (both about 0.42) are much higher than that in the Bottom type (i.e., 0.19). The distinct features of aerosol vertical distribution and largely varied aerosol loadings in different aerosol vertical types between the two ARM sites can apparently affect the aerosol-cloud relations, which will be examined in the following sections.

3.2. Impacts of aerosol vertical distributions on aerosol-cloud interactions

3.2.1. Cloud macro- and microphysical responses

To assess the association between warm cloud macro- and microphysics and aerosol loadings, we divided the available aerosol-cloud collocation samples into several bins according to the probability density function (PDF) of AOD that the sample number is nearly evenly distributed across AOD bins. Different AOD bins represent various aerosol pollution levels, i.e., from clean to polluted conditions. Then the responses of cloud macro- and microphysical parameters to the increase in AOD were evaluated with respect to aerosol vertical types. The examined cloud feature parameters include cloud geometric thickness, LWC, LWP, COD, cloud extinction coefficient (β_e), and droplet effective radius (R_e), as well as cloud top and base heights.

Figs. 5 and 6 illustrate the correlation curves of key cloud feature parameters in response to AOD in the three primary vertical types at SGP and ENA, respectively. From Fig. 5a and b, it is found that both the responses of cloud thickness and LWC to AOD at SGP vary with aerosol vertical types. For example, the cloud geometric thickness in the Random type shows a monotonically increasing trend as AOD increases but displays a "A"-shaped curve in the Decreasing type, i.e., firstly increasing with AOD at a smaller range and then decreasing at a larger AOD range (Fig. 5a). In the Bottom type, the cloud thickness fluctuates up and down at relatively small AOD levels and then increases with AOD until the large AOD end. The curve shapes for LWC responding to AOD are also very different across aerosol vertical types. The LWC in the Decreasing type shows a clear "V"-shaped response, i.e., the LWC decreases until AOD reaching 0.35 and then starts to increase for AOD larger than 0.35 (Fig. 5b). In the Random type, the LWC increases with AOD when AOD < 0.3 but decreases when AOD > 0.3. It is also found that the LWP response in general resembles the LWC response (Fig. 5b and c). As LWP is a product of LWC and cloud thickness, the similarity between the LWP and LWC responses implies that the LWC changes caused by aerosols dominate over the cloud thickness changes at SGP.

At ENA, a monotonic increase is observed for the cloud thickness in both the Decreasing and Random types, but a non-monotonic response is shown in the Bottom type (Fig. 6a). The geometrically thickening of cloud layer in the Decreasing and Random types suggests that the aerosol effect invigorates cloud development vertically, which is also evident in the enhanced cloud top height with aerosols (Fig. S1). The relations between LWC and AOD also vary with aerosol vertical types, with a slight decreasing in the Decreasing type and "A" shapes in both the Random and Bottom types (Fig. 6b). Because of the combined effect

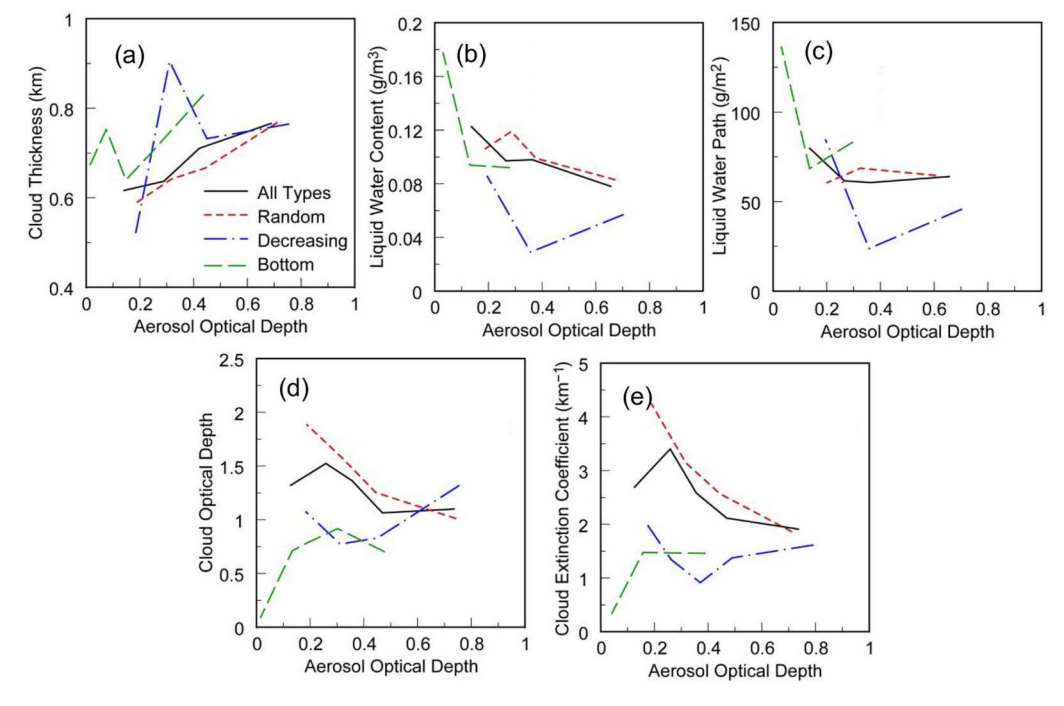


Fig. 5. Changes in cloud properties of (a) cloud thickness, (b) layer-mean liquid water content, (c) liquid water path, (d) cloud optical depth, and (e) cloud extinction coefficient with column aerosol optical depth in different aerosol vertical types, including All (black solid), Random (red dash), Decreasing (blue dash), and Bottom (green dash) at the SGP site.

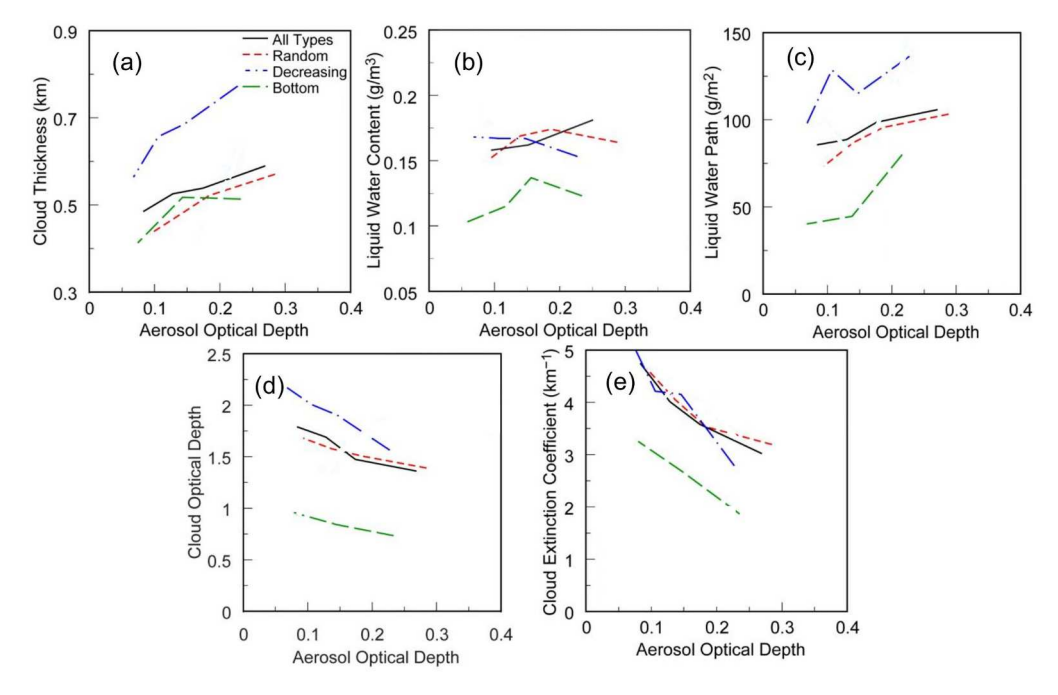


Fig. 6. Same as Fig. 5 except for the ENA site.

of cloud thickness and LWC, the LWP response is complex and highly dependent on aerosol vertical type as well (Fig. 6c). For instance, in the Bottom and Random types the LWP presents a monotonic increasing response to AOD, but in the Decreasing type it shows a zigzag-shaped response. Therefore, we conclude that the aerosol vertical distribution can considerably modulate the monotonicity of cloud responses to AOD changes.

More interestingly, the effect of aerosol vertical distribution can alter the relations between COD and AOD particularly at SGP. The response of COD in the Random type shows a monotonic decreasing, but it presents a "V" and " Λ "-shaped variation in the Decreasing and Bottom types, respectively (Fig. 5d). Although COD is the product of cloud thickness and β_e , its response to aerosols is similar to that of β_e in all the vertical types (Fig. 5e). The similarity of the responses between COD and β_e to AOD is also the case at ENA, i.e., the monotonic decreasing of COD with AOD is consistent with the decline of β_e (Fig. 6d and e). Therefore, the changes in COD with AOD is primarily driven by the variation of cloud extinction coefficient caused by the aerosol effect.

To more quantitatively measure aerosol-cloud interaction, we employed two indicators, i.e., relative liquid water sensitivity and aerosol-cloud interaction (ACI) index by using the least squares linear regression on all available data points. Relative liquid water sensitivity is defined as the ratio of $\partial ln(LWP)$ to $\partial ln(AOD)$. ACI index relative to cloud droplet effective radius (ACI_{Re}) is defined as the ratio of $\partial ln(R_e)$ to $\partial ln(AOD)$, which is then multiplied with -1 to ensure a positive value when the Twomey effect occurs, i.e.

$$ACI_{R_{e}} = -\frac{\partial ln(R_{e})}{\partial ln(AOD)}\bigg|_{LWP}.$$
(3)

To eliminate the possible bias caused by the Re dependence on LWP when evaluating the Twomey effect, ACI_{Re} should be calculated at a constant LWP (Feingold et al., 2003; Garrett et al., 2004; Zheng et al., 2020). According to the ranges of LWP and the number of data points, we divided all LWP samples into two bins when deriving ACI_{Re}, i.e., 0–50 g m $^{-2}$ (hereafter low-LWP conditions) and 50–150 g m $^{-2}$ (hereafter high-LWP conditions).

Fig. 7a shows that the relative liquid water sensitivity in general is negative at SGP, and the means with 95 % confidence intervals are -0.23 ± 0.31 , -0.25 ± 0.83 , 0.00 ± 0.34 , and -0.15 ± 0.18 for the

Bottom, Decreasing, Random and All types, respectively. This suggests that LWP tends to be reduced in high aerosol conditions at SGP, but this cloud suppression effect is not statistically significant because of the relatively large uncertainties (e.g., in the Decreasing and Random types). In contrast, the relative liquid water sensitivity is generally positive at ENA, and the means with 95 % confidence intervals are 0.21 \pm 0.45, 0.03 \pm 0.26, 0.21 \pm 0.14, and 0.14 \pm 0.12 for the Bottom, Decreasing, Random and All types, respectively. Therefore, the aerosols tend to invigorate cloud water production at ENA, which is particularly significant in the Random type because of the relatively small uncertainty (0.14) with respect to its mean (0.21).

The differences in cloud susceptibility to aerosols among different aerosol vertical types and between the two sites might imply the distinct mechanisms of aerosol effects with respect to aerosol vertical distribution and environmental conditions. For example, in the Decreasing type at SGP the reduced cloud water amount with increasing aerosols can be driven by the decoupling of cloud layer from the boundary layer, which is due to the evaporative cooling by small droplets under polluted conditions (Han et al., 2002). Decoupling of cloud layer can result in less efficient water vapor delivery from lower boundary layer into the clouds. Aerosol semi-direct effect, i.e., burning off cloud droplets in cloud layer by the heating of absorbing aerosols, may also contribute to the less production of cloud water in the Decreasing type, which is with smaller droplets under more polluted aerosol condition (Hansen et al., 1997; Herbert et al., 2020). At ENA, the drizzle suppression by aerosols (i.e., Albrecht effect, Albrecht, 1989) may be responsible for the cloud water enhancement in the Decreasing type.

Note that in the Bottom type the top height of aerosol layer is lower than the cloud base height at both sites (Fig. S2), suggesting that aerosols in Bottom may have low chance of entering clouds. As such, the strong correlations between cloud properties and AOD in the Bottom type may not be attributed to the aerosol microphysical effect but to the aerosol radiative effect. For example, in the Bottom type at ENA, the heating effect of absorbing aerosol below the cloud layer could play a dominant role in enhancing the cloud water by causing stronger convection underneath the cloud layer, which is favorable for cloud development. However, the negative liquid water sensitivity in the Bottom and Random types at SGP still needs further investigation. Because there are appreciable aerosols present above, in, and below

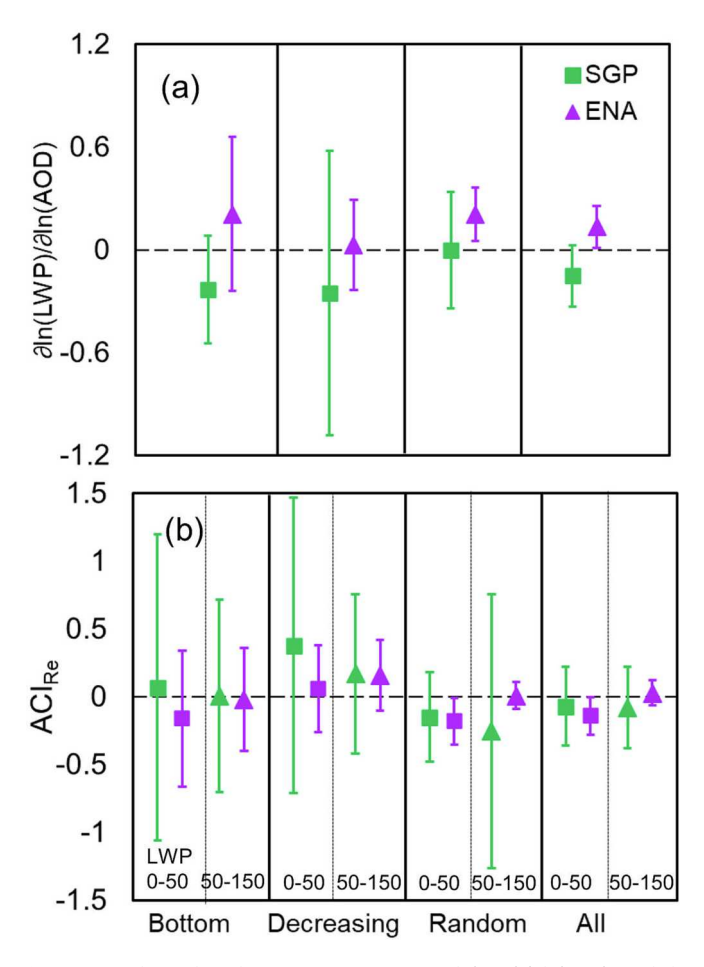


Fig. 7. (a) Relative liquid water sensitivity (i.e., $\partial ln(LWP)/\partial ln(AOD)$) and (b) aerosol-cloud interaction index (ACI_{Re}) with respect to cloud droplet effective radius and AOD (i.e., $-\partial ln(Re)/\partial ln(AOD)$) at the LWP ranges of 0–50 g m⁻² and 50–150 g m⁻² at SGP (green) and ENA (purple). From left to right are Bottom, Decreasing, Random, and All aerosol types. Vertical lines denote 95 % confidence intervals.

cloud layer in the Random type, aerosol radiative, semi-direct, and CCN effects likely work simultaneously and thus their combined effect may be responsible for the complexity of aerosol-cloud interactions observed at both SGP and ENA in this specific aerosol vertical type.

Fig. 7b shows that the ACIRe varies with aerosol vertical types, observation locations, and LWP levels. In either bin of LWP, the mean ACIRe is positive in Decreasing but negative in Random over SGP. Since the ACI_{Re} describes the response of R_e to aerosol loadings, the positive ACIRe suggests that the droplets' size is reduced in the decreasing type when more aerosols are introduced into the atmosphere, i.e., the Twomey effect, while the negative ACIRe indicates the droplets' size is enlarged at elevated aerosol loadings, i.e., the Anti-Twomey effect. However, the Twomey or Anti-Twomey effect over SGP is relatively weak because of the large uncertainties of those ACIRe (i.e., see the large 95 % confidence intervals in Fig. 7b). The ACI_{Re} over ENA tends to be negative in both the Bottom and Random types under low-LWP conditions and positive in the Decreasing type under high-LWP conditions. The negative ACI_{Re} in the Random type is particularly statistically significant because of its relatively small confidence interval, which indicates the strong Anti-Twomey effect in this case. The Anti-Twomey effect is observed in several situations in our study, particularly in the Random type at either site under low-LWP conditions. Several possible physical mechanisms have been suggested by previous studies to interpret why the Anti-Twomey effect happens (Jose et al., 2020; Liu et al., 2021; Liu et al., 2020; Yuan et al., 2008), e.g., a decrease in CCN number

with an increasing slightly soluble organics content in aerosols or the water vapor competition effect among giant CCNs and other regular CCNs. In the latter case, activation of giant CCNs can sufficiently reduce the supersaturation and as a result the small droplets could evaporate more quickly. A recent study by Yang et al. (2021) suggested that the existence of drizzle particles within clouds can enlarge the cloud droplet effective radius via efficient collision-coalescence among these drizzle particles, making the droplets' size even increasing with aerosol amount. Given the various sources of aerosols and complicated cloud conditions at the two sites, these mechanisms could be applied to elaborate the Anti-Twomey effect observed in this study, but detailed information on aerosol chemical components and particle size is needed to further specify which physical pathway indeed plays a role.

In addition, we find that under low-LWP conditions the ACI_{Re} values are generally larger at SGP than at ENA, suggesting that aerosols tend to show the more Twomey effect at SGP compared to ENA. One possible reason is that the aerosol first indirect effect is manifested in the drier and more polluted continental environment, like SGP, where LWP is relatively low. We also find that the mean ACIRe over SGP is reduced at high-level LWP but generally enhanced over ENA. Zheng et al. (2020) observed the similar decreasing trend of ACIRe with LWP at SGP and hypothesized some physical understandings: Smaller droplets under low-LWP conditions compete against each other for the limited water available in the boundary layer, which is likely the case at a continental site like SGP, and therefore Re is more sensitive to perturbed aerosols; however, under high-LWP conditions smaller droplets can grow efficiently via condensation because of relatively sufficient water vapor supply but the grow efficacy declines with the enlarged droplets' size, leading to reduced variations of Re for similar aerosol loadings change. In contrast, the ENA site normally has high moisture but low aerosols loadings compared to SGP, which is responsible for the very different relation between Re and AOD from SGP. However, the detailed physical processes leading to the increasing trends of ACIRe at ENA still need more elaboration in future.

3.2.2. Influence of meteorology covariation

To examine the possible influence of meteorological variations, the relationships of two cloud parameters, i.e., COD and LWP, with AOD plotted separately with respect to meteorological parameters interested are illustrated in Figs. 8, 9, S3, and S4. For some meteorological parameters, the curve shapes are in general similar under different meteorological regimes, e.g., the "V"-shaped LWP-AOD relations for all the three regimes of T750-850hPa and CAPE at SGP (Fig. S3d and f), and the monotonic decreasing responses of COD to AOD for all the three regimes of RH_{750-850hPa} and LTS_{700hPa} at ENA (Fig. 9a and b). However, in most situations the curve shapes of cloud-AOD relations show distinct features among the three meteorological regimes. For example, the relations of COD with AOD at SGP can change greatly in different regimes of all the examined meteorological parameters (Figs. 8a-c and S3a-c), and the LWP-AOD relations at SGP can vary significantly according to the LTS_{700hPa} and VV_{750-850hPa} regimes (Figs. 8e and S3e). Specifically, the SGP COD/LWP increasing/decreasing trend with AOD in the small LTS_{700hPa} range (i.e., <10.4 K in Fig. 8b or <14.4 K in Fig. 8e) is reversed to decreasing/increasing in the large LTS_{700hPa} range (i.e., $>\!\!14.8$ K in Fig. 8b or >18.4 K in Fig. 8e). At ENA, the slope signs and magnitudes as well as the response monotonicity are dependent on the meteorology regimes for all LWP-AOD relations (Figs. 9d-f and S4d-f). Previous studies have reported that there could be a strong dependency of cloud microphysics-AOD relationships on meteorological conditions (e.g., Altaratz et al., 2014, Mauger and Norris, 2007, Koren et al., 2010, Varble, 2018, Zhao et al., 2018a); in this study for warm clouds, we also demonstrate this is likely the case. Therefore, the correlations observed above cannot only be attributed to aerosol effect but may also be due to the covariations of AOD and cloud with meteorological conditions.

To isolate the aerosol effect from the contribution of metrological covariations, we further binned the observed COD and LWP according to

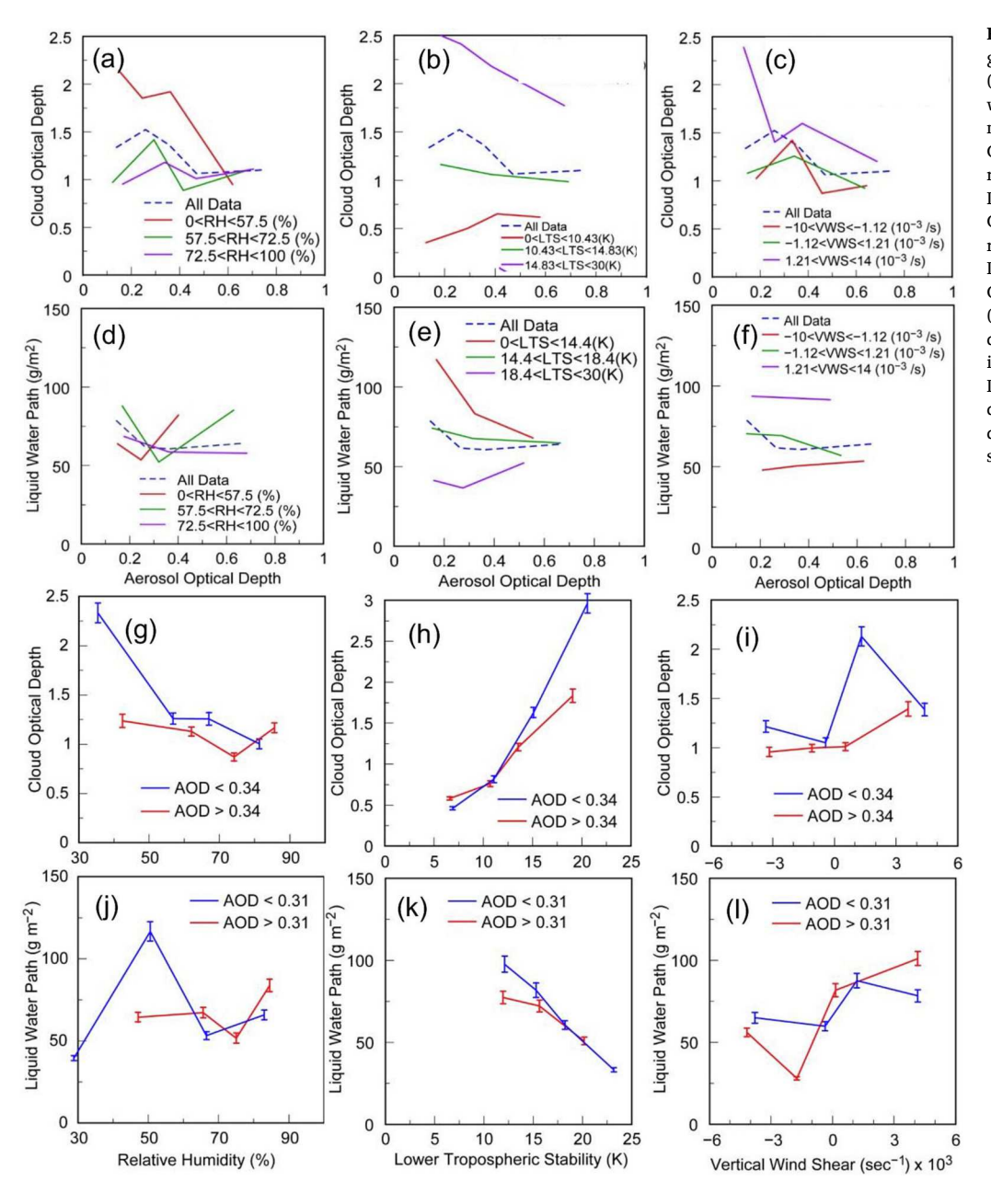


Fig. 8. Influence of aerosols on (a-c, g-i) cloud optical depth (COD) and (d-f. i-l) liquid water path (LWP) of warm clouds at SGP modulated by meteorological conditions. (a-c)Changes in COD with AOD for different ranges of (a) RH_{750-850hPa}, LTS_{700hPa}, and (c) VWS_{725-925hPa}. (d-f) Changes in LWP with AOD for different ranges of (d) RH_{750-850hPa}, LTS_{700hPa}, and (f) VWS_{725-925hPa}. (g-i) Changes in COD with (g) RH750-850hPa, (h) LTS $_{700hPa}$, and (i) VWS $_{725-925hPa}$ for different ranges of AOD. (i-l) Changes in LWP with (j) $RH_{750-850hPa}$, (k) LTS_{700hPa}, and (l) VWS_{725-925hPa} for different ranges of AOD. Vertical lines denote the error bars for one sigma standard deviation.

meteorology parameters under different ranges of AODs (Figs. 8g-l, 9g-l, S3g-l, and S4g-l). As illustrated by RH_{750-850hPa} from Figs. 8g and 9g, the COD is reduced as AOD increases from <0.34 (or 0.15) to >0.34(or 0.15) at SGP (or ENA) for a given value of RH_{750-850hPa}, suggesting the role of aerosols in altering cloud optical property when the moisture condition holds constant. In Fig. 8h, a larger AOD corresponds to a larger COD for a given LTS within LTS < 10 K while a larger AOD leads to a smaller COD for a given LTS within LTS > 10 K, suggesting a relatively significant impacts of aerosols on modifying cloud optical property. Similar results are found for LWP with respect to LTS_{700hPa}, T_{750-850hPa}, VV_{750-850hPa}, and CAPE at both sites (the panels of k and l of Figs. 8 and 9, and the panels j and l of in Figs. S3 and S4). Moreover, the changes in COD and LWP induced by aerosols could be opposite under a certain given meteorological condition, e.g., LTS_{700hPa}, VWS_{725-925hPa}, T₇₅₀₋ 850hPa, VV_{750-850hPa}, and CAPE (Figs. 8h, j, l, S3g, j, k, l, and S4 h and l). Considerable changes in cloud properties from small to large AOD are evident for most meteorology parameters examined, which demonstrates the role of aerosols in modulating COD and LWP under the same

meteorological conditions. Therefore, the strong negative or positive correlations between cloud macro- and microphysics and AOD observed above can be attributed, at least partially, to the aerosol effect.

4. Conclusions

In this study, we investigated the characteristics of aerosol vertical distributions at the U.S. DOE ARM atmospheric observatories (i.e., SGP and ENA) and the impacts of aerosol vertical distributions on warm cloud properties by using the 2016–2020 and 2015–2021 measurements of aerosol vertical profiles from Raman Lidar systems at the two sites. ARM VAPs of cloud features were obtained from the ARM facility as well. The observation-based analysis reveals significant seasonality and diurnal variation of aerosol vertical distributions, which is largely dependent of the observation geolocations. Specifically, the columnintegrated AOD shows a nearly unimodal distribution with a peak in summer at SGP, which is attributed to the seasonal variation of the AODs above 1000 m (a.g.l.). In contrast, a bimodal seasonal distribution of the

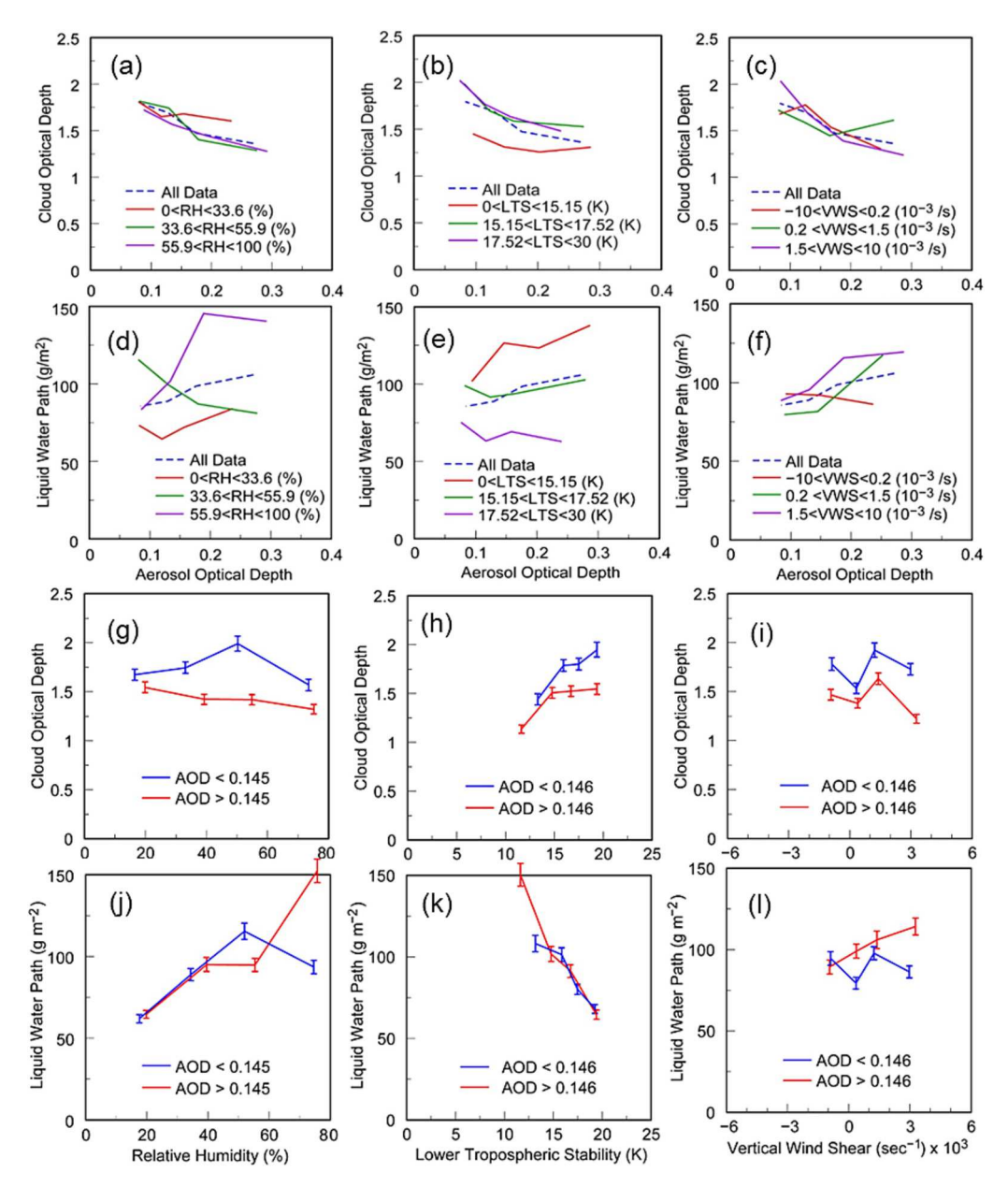


Fig. 9. Same as Fig. 8 but for the ENA site.

integrated AOD is observed at ENA, with a major peak in late winter/early spring and a minor one in fall. The column AOD seasonality at ENA is controlled by the AODs of vertical levels both below and above 800 m (a.g.l.), given that the AODs of vertical levels above 800 m also present a spike in summer. The seasonal-mean aerosol layer at SGP can extend vertically as high as 5 km, but aerosols at ENA generally are confined below 2 km. It is also found that a clear diurnal cycle of AOD is observed at SGP, with a peak in the evening (at about 18:00 LT) and a valley at late night (at about 3:00 LT) and a relative range of diurnal variation of about 40 %. This diurnal cycle is attributed to the diurnal variation of AODs of the vertical layers above 1000 m (a.g.l.). There is no clear diurnal cycle at ENA.

Aerosol profiles and cloud systems were collocated using the timing information of their passage over the two sites, and three primary aerosol vertical distribution types were identified based on the relative positions of the collocated aerosol layers to clouds. The Random, Decreasing, and Bottom types account for $74.3\,\%$, $12.7\,\%$, and $12.7\,\%$ of total cases over SGP, and $70.0\,\%$, $22.9\,\%$, and $6.1\,\%$ of total cases over ENA, respectively.

With aerosol-cloud collocation and its classification, the correlations between cloud macro- and microphysical parameters and aerosol loadings (taking AOD as the proxy) were comprehensively evaluated. We find that aerosols can alter cloud macro- and microphysics, which is strongly dependent on aerosol vertical types and observation geolocations. For example, aerosols can geometrically thicken the cloud layer in Random at SGP and in both Random and Decreasing at ENA, suggesting an invigoration effect on cloud vertical development in these situations. Non-linear and complex changes in cloud layer thickness with AOD are shown in both Bottom and Decreasing at SGP and in Bottom at ENA. It is interesting to see that aerosol vertical distribution can greatly modulate the relations between COD and AOD, and instead of cloud thickness, it is the variation of cloud extinction coefficient which primarily drives the changes in cloud COD caused by the aerosol effect. The observed liquid water sensitivity (\partial ln(LWP)/\partial ln(AOD)) is negative at SGP in the Bottom and Random types, i.e., aerosols tend to suppress liquid cloud water production in continental boundary condition. In contrast, the LWPs increase with AOD at ENA, which is particularly significant in the Random type, suggesting that aerosols tend to

enhance cloud water formation under marine boundary condition. At both sites we find that the aerosol vertical distribution can considerably modulate the monotonicity of cloud responses to AOD changes.

Moreover, the relations of cloud droplet effective radius (Re) with AOD, as indicated by ACI_{Re}, largely depends on aerosol vertical types, observation locations, and LWP levels. In both LWP bins (i.e., 0-50 g m^{-2} and 50–150 g m^{-2}), the mean ACI_{Re} are positive in Decreasing but negative in Random over SGP. The ACI_{Re} over ENA is positive in Decreasing under high-LWP conditions but negative in both Bottom and Random under low-LWP conditions. The negative ACIRe, representing the Anti-Twomey effect, is observed in several situations in this study at both sites, particularly in the Random type. It is also found that under low-LWP conditions, the ACI_{Re} normally is larger at SGP than at ENA. In addition, the mean ACIRe over SGP decreases with an increase in LWP but increases over ENA. The different responses of warm cloud properties to aerosols between SGP and ENA are in relation to aerosol vertical distributions, which are likely a result of the ocean-continent contrast in thermodynamic and aerosol conditions where clouds form. Our further analyses demonstrate that aerosols are still effective in modulating cloud properties after ruling out the covarying effect of meteorological

This work highlights that an accurate representation of aerosol vertical distribution is required to reduce the uncertainty in future evaluation of aerosol-warm cloud interactions. However, given the uncertainties of lidar measurements and feature detection, further cross-validations based on other observations, e.g., airborne or spaceborne measurements, are needed. Moreover, the mechanisms through which aerosol vertical distribution can affect the warm cloud properties still require further elucidation and modeling in future, particularly considering the complexity of aerosol microphysical and radiative effects under different thermodynamic conditions.

CRediT authorship contribution statement

YG, YT, and YL conceived and designed the study; YL, YT, SZ, and KZ collected and analyzed the data; YL, YT, and YG wrote the manuscript draft; YW, TZ, JW, BZ, GC, DZ, RF, and JS reviewed and edited the manuscript.

Declaration of competing interest

The authors declare that they have no known competing financial interests or personal relationships that could have appeared to influence the work reported in this paper.

Data availability

Data will be made available on request.

Acknowledgments

This work was supported by the NSF grants AGS-2103820 and AGS-2103714, NASA ROSES TASNPP (80NSSC18K0985) and CCST (80NSSC23K0119) grants. Y. G. acknowledges the support by (while serving at) the National Science Foundation. We would like to acknowledge high-performance computing support from Cheyenne (doi:10.5065/D6RX99HX) provided by NCAR's Computational and Information Systems Laboratory, sponsored by the National Science Foundation.

Appendix A. Supplementary data

Supplementary data to this article can be found online at https://doi.org/10.1016/j.scitoteny.2023.166582.

References

- Ackerman, T.P., Stokes, G.M., 2003. The atmospheric radiation measurement program. Phys. Today 56, 38–44. https://doi.org/10.1063/1.1554135.
- Albrecht, B.A., 1989. Aerosols, cloud microphysics, and fractional cloudiness. Science 245, 1227–1230. https://doi.org/10.1126/science.245.4923.1227.
- Altaratz, O., Bar-Or, R.Z., Wollner, U., Koren, I., 2013. Relative humidity and its effect on aerosol optical depth in the vicinity of convective clouds. Environ. Res. Lett. 8, 034025 https://doi.org/10.1088/1748-9326/8/3/034025.
- Altaratz, O., Koren, I., Remer, L.A., Hirsch, E., 2014. Review: cloud invigoration by aerosols—coupling between microphysics and dynamics. Atmos. Res. 140-141, 38-60. https://doi.org/10.1016/j.atmosres.2014.01.009.
- Balmes, K.A., Fu, Q., Thorsen, T.J., 2019. Differences in ice cloud optical depth from CALIPSO and ground-based Raman Lidar at the ARM SGP and TWP sites. J. Geophys. Res. 124, 1755–1778. https://doi.org/10.1029/2018JD028321.
- Boucher, O.R.D., Artaxo, P., Bretherton, C., Feingold, G., Forster, P., Kerminen, V.-M., Kondo, Y., Liao, H., Lohmann, U., Rasch, P., Satheesh, S.K., Sherwood, S., Stevens, B., Zhang, X.Y., 2013. Clouds and aerosols. In: Climate Change 2013: The Physical Science Basic. Cambridge University Press, Cambridge, United Kingdom and New York
- Boyouk, N., Léon, J.-F., Delbarre, H., Podvin, T., Deroo, C., 2010. Impact of the mixing boundary layer on the relationship between PM2.5 and aerosol optical thickness. Atmos. Environ. 44, 271–277. https://doi.org/10.1016/j.atmosenv.2009.06.053.
- Carslaw, K.S., Boucher, O., Spracklen, D.V., Mann, G.W., Rae, J.G.L., Woodward, S., et al., 2010. A review of natural aerosol interactions and feedbacks within the earth system. Atmos. Chem. Phys. 10, 1701–1737. https://doi.org/10.5194/acp-10-1701-2010.
- Chand, D., Wood, R., Anderson, T.L., Satheesh, S.K., Charlson, R.J., 2009. Satellite-derived direct radiative effect of aerosols dependent on cloud cover. Nat. Geosci. 2, 181–184. https://doi.org/10.1038/ngeo437.
- Chand, D., Wood, R., Ghan, S.J., Wang, M.H., Ovchinnikov, M., Rasch, P.J., et al., 2012. Aerosol optical depth increase in partly cloudy conditions. J. Geophys. Res.-Atmos. 117, D17207 https://doi.org/10.1029/2012jd017894.
- Chand, D., Newsome, R., Thorsen, T., Cromwell, E., Sivaraman, C., Flynn, C., Shilling, J., Comstock, J., 2019. Aerosol and Cloud Optical Properties from the ARM Raman Lidars: The Feature Detection and Extinction (FEX) Value-Added Product, Vol. DOE/ SC-ARM-TR-224. U.S. Department of Energy.
- Chen, Y.-C., Christensen, M.W., Stephens, G.L., Seinfeld, J.H., 2014. Satellite-based estimate of global aerosol–cloud radiative forcing by marine warm clouds. Nat. Geosci. 7, 643–646. https://doi.org/10.1038/ngeo2214.
- Chen, A., Zhao, C., Fan, T., 2022. Spatio-temporal distribution of aerosol direct radiative forcing over mid-latitude regions in north hemisphere estimated from satellite observations. Atmos. Res. 266, 105938 https://doi.org/10.1016/j. atmosres.2021.105938.
- Chen, A., Zhao, C., Shen, L., Fan, T., 2023. Influence of aerosol properties and surface albedo on radiative forcing efficiency of key aerosol types using global AERONET data. Atmos. Res. 282, 106519 https://doi.org/10.1016/j.atmosres.2022.106519.
- Chung, C.E., Ramanathan, V., Kim, D., Podgorny, I.A., 2005. Global anthropogenic aerosol direct forcing derived from satellite and ground-based observations. J. Geophys. Res. 110, D24207 https://doi.org/10.1029/2005jd006356.
- Costantino, L., Bréon, F.-M., 2013. Aerosol indirect effect on warm clouds over south-East Atlantic, from co-located MODIS and CALIPSO observations. Atmos. Chem. Phys. 13, 69–88. https://doi.org/10.5194/acp-13-69-2013.
- De Reus, M., Ström, J., Curtius, J., Pirjola, L., Vignati, E., Arnold, F., et al., 2000. Aerosol production and growth in the upper free troposphere. J. Geophys. Res. 105, 24751–24762. https://doi.org/10.1029/2000jd900382.
- Diamond, M.S., Dobracki, A., Freitag, S., Small Griswold, J.D., Heikkila, A., Howell, S.G., et al., 2018. Time-dependent entrainment of smoke presents an observational challenge for assessing aerosol-cloud interactions over the southeast Atlantic Ocean. Atmos. Chem. Phys. 18, 14623–14636. https://doi.org/10.5194/acp-18-14623-2019.
- Ding, A.J., Huang, X., Nie, W., Sun, J.N., Kerminen, V.-M., Petäjä, T., et al., 2016. Enhanced haze pollution by black carbon in megacities in China. Geophys. Res. Lett. 43, 2873–2879. https://doi.org/10.1002/2016GL067745.
- Dubovik, O., Herman, M., Holdak, A., Lapyonok, T., Tanre, D., Deuze, J.L., et al., 2011a. Statistically optimized inversion algorithm for enhanced retrieval of aerosol properties from spectral multi-angle polarimetric satellite observations. Atmos. Meas. Tech. 4, 975–1018. https://doi.org/10.5194/amt-4-975-2011.
- Dubovik, O., Herman, M., Holdak, A., Lapyonok, T., Tanré, D., Deuzé, J.L., et al., 2011b. Statistically optimized inversion algorithm for enhanced retrieval of aerosol properties from spectral multi-angle polarimetric satellite observations. Atmos. Meas. Tech. 4, 975–1018. https://doi.org/10.5194/amt-4-975-2011.
- Fan, J., Liu, Y.-C., Xu, K.-M., North, K., Collis, S., Dong, X., et al., 2015. Improving representation of convective transport for scale-aware parameterization: 1. Convection and cloud properties simulated with spectral bin and bulk microphysics. J. Geophys. Res. 120, 2014JD022142 https://doi.org/10.1002/2014JD022142.
- Feingold, G., Eberhard, W.L., Veron, D.E., Previdi, M., 2003. First measurements of the Twomey indirect effect using ground-based remote sensors. Geophys. Res. Lett. 30, 1287. https://doi.org/10.1029/2002gl016633.
- Gadhavi, H., Jayaraman, A., 2006. Airborne lidar study of the vertical distribution of aerosols over Hyderabad, an urban site in central India, and its implication for radiative forcing calculations. Ann. Geophys. 24, 2461–2470. https://doi.org/ 10.5194/angep-24-2461-2006.
- Garrett, T.J., Zhao, C., Dong, X., Mace, G.G., Hobbs, P.V., 2004. Effects of varying aerosol regimes on low-level Arctic stratus. Geophys. Res. Lett. 31, L17105 https://doi.org/ 10.1029/2004GL019928.

- Gu, Y., Liou, K.N., Xue, Y., Mechoso, C.R., Li, W., Luo, Y., 2006. Climatic effects of different aerosol types in China simulated by the UCLA general circulation model. J. Geophys. Res.-Atmos. 111, D15201 https://doi.org/10.1029/2005jd006312.
- Gu, Y., Liou, K.N., Chen, W., Liao, H., 2010. Direct climate effect of black carbon in China and its impact on dust storms. J. Geophys. Res. 115, D00K14 https://doi.org/ 10.1029/2009jd013427.
- Gu, Y., Xue, Y., De Sales, F., Liou, K.N., 2016. A GCM investigation of dust aerosol impact on the regional climate of North Africa and south/East Asia. Clim. Dyn. 46, 2353–2370. https://doi.org/10.1007/s00382-015-2706-y.
- Han, Q., Welch, R., Chou, J., Rossow, W., White, A., 1995. Validation of satellite retrievals of cloud microphysics and liquid water path using observations from FIRE. J. Atmos. Sci. 52, 4183–4195. https://doi.org/10.1175/1520-0469(1995) 052<4183:vosroc>2.0.co;2.
- Han, Q., Rossow, W.B., Zeng, J., Welch, R., 2002. Three different behaviors of liquid water path of water clouds in aerosol–cloud interactions. J. Atmos. Sci. 59, 726–735. https://doi.org/10.1175/1520-0469(2002)059<0726:tdbolw>2.0.co;2.
- Hansen, J., Sato, M., Ruedy, R., 1997. Radiative forcing and climate response.
 J. Geophys. Res. 102, 6831–6864. https://doi.org/10.1029/96jd03436.
- Haywood, J., Boucher, O., 2000. Estimates of the direct and indirect radiative forcing due to tropospheric aerosols: a review. Rev. Geophys. 38, 513–543. https://doi.org/ 10.1029/1999rg000078.
- Herbert, R.J., Bellouin, N., Highwood, E.J., Hill, A.A., 2020. Diurnal cycle of the semi-direct effect from a persistent absorbing aerosol layer over marine stratocumulus in large-eddy simulations. Atmos. Chem. Phys. 20, 1317–1340. https://doi.org/10.5194/acp-20-1317-2020.
- Hsu, N.C., Tsay, S.C., King, M.D., Herman, J.R., 2004. Aerosol properties over bright-reflecting source regions. IEEE Trans. Geosci. Remote Sens. 42, 557–569. https://doi.org/10.1109/Tgrs.2004.824067.
- Huang, L., Jiang, J.H., Tackett, J.L., Su, H., Fu, R., 2013. Seasonal and diurnal variations of aerosol extinction profile and type distribution from CALIPSO 5-year observations. J. Geophys. Res.-Atmos. 118, 4572–4596. https://doi.org/10.1002/ jgrd.50407.
- Huebert, B.J., Howell, S.G., Zhuang, L., Heath, J.A., Litchy, M.R., Wylie, D.J., et al., 1998. Filter and impactor measurements of anions and cations during the first aerosol characterization experiment (ACE 1). J. Geophys. Res. 103, 16493–16509. https://doi.org/10.1029/98id00770.
- Huige, D., Siwen, L., Yun, Y., Dengxin, H., Jianyu, W., 2021. Observational study of the vertical aerosol and meteorological factor distributions with respect to particulate pollution in Xi'an. Atmos. Environ. 247, 118215 https://doi.org/10.1016/j. atmosenv.2021.118215.
- Johnson, B.T., Shine, K.P., Forster, P.M., 2004. The semi-direct aerosol effect: impact of absorbing aerosols on marine stratocumulus. Q. J. R. Meteorol. Soc. 130, 1407–1422. https://doi.org/10.1256/gi.03.61.
- Johnson, B.T., Heese, B., Mcfarlane, S.A., Chazette, P., Jones, A., Bellouin, N., 2008.
 Vertical distribution and radiative effects of mineral dust and biomass burning aerosol over West Africa during DABEX. J. Geophys. Res. 113, D00C12 https://doi.org/10.1029/2008jd009848.
- Jose, S., Nair, V.S., Babu, S.S., 2020. Anthropogenic emissions from South Asia reverses the aerosol indirect effect over the northern Indian Ocean. Sci. Rep. 10, 18360. https://doi.org/10.1038/s41598-020-74897-x.
- Kahn, R.A., 2012. Reducing the uncertainties in direct aerosol radiative forcing. Surv. Geophys. 33, 701–721. https://doi.org/10.1007/s10712-011-9153-z.
- Kaufman, Y.J., Tanré, D., Boucher, O., 2002. A satellite view of aerosols in the climate system. Nature 419, 215–223. https://doi.org/10.1038/nature01091.
- Kaufman, Y.J., Koren, I., Remer, L.A., Rosenfeld, D., Rudich, Y., 2005. The effect of smoke, dust, and pollution aerosol on shallow cloud development over the Atlantic Ocean. Proc. Natl. Acad. Sci. U. S. A. 102, 11207–11212. https://doi.org/10.1073/ pnas.0505191102.
- Kim, M.-H., Omar, A.H., Vaughan, M.A., Winker, D.M., Trepte, C.R., Hu, Y., et al., 2017. Quantifying the low bias of CALIPSO's column aerosol optical depth due to undetected aerosol layers. J. Geophys. Res. 122, 1098–1113. https://doi.org/ 10.1002/2016id025797.
- Klein, S.A., Hartmann, D.L., 1993. The seasonal cycle of low stratiform clouds. J. Clim. 6, 1587–1606. https://doi.org/10.1175/1520-0442(1993)006<1587:tscols>2.0.co;2.
- Kokhanovsky, A.A., Deuzé, J.L., Diner, D.J., Dubovik, O., Ducos, F., Emde, C., et al., 2010. The inter-comparison of major satellite aerosol retrieval algorithms using simulated intensity and polarization characteristics of reflected light. Atmos. Meas. Tech. 3, 909–932. https://doi.org/10.5194/amt-3-909-2010.
- Koren, I., Feingold, G., Remer, L.A., 2010. The invigoration of deep convective clouds over the Atlantic: aerosol effect, meteorology or retrieval artifact? Atmos. Chem. Phys. 10, 8855–8872. https://doi.org/10.5194/acp-10-8855-2010.
- Lee, J., Hsu, N.C., Bettenhausen, C., Sayer, A.M., Seftor, C.J., Jeong, M.J., 2015. Retrieving the height of smoke and dust aerosols by synergistic use of VIIRS, OMPS, and CALIOP observations. J. Geophys. Res.-Atmos. 120, 8372–8388. https://doi.org/10.1002/2015jd023567.
- Léon, J.-F., 2002. Aerosol direct radiative impact over the INDOEX area based on passive and active remote sensing. J. Geophys. Res. 107 (D19), 8006. https://doi.org/ 10.1029/2000jd000116.
- Levy, R.C., Remer, L.A., Mattoo, S., Vermote, E.F., Kaufman, Y.J., 2007. Second-generation operational algorithm: retrieval of aerosol properties over land from inversion of moderate resolution imaging Spectroradiometer spectral reflectance.
 J. Geophys. Res.-Atmos. 112, D13211 https://doi.org/10.1029/2006jd007811.
- Li, Z., Zhao, X., Kahn, R., Mishchenko, M., Remer, L., Lee, K.-H., et al., 2009. Uncertainties in satellite remote sensing of aerosols and impact on monitoring its long-term trend: a review and perspective. Ann. Geophys. 27, 2755–2770. https://doi.org/10.5194/angeo-27-2755-2009.

- Li, Z., Guo, J., Ding, A., Liao, H., Liu, J., Sun, Y., et al., 2017. Aerosol and boundary-layer interactions and impact on air quality. Natl. Sci. Rev. 4, 810–833. https://doi.org/ 10.1093/nsr/nwx117
- Liang, Q., Jaeglé, L., Jaffe, D.A., Weiss-Penzias, P., Heckman, A., Snow, J.A., 2004. Long-range transport of Asian pollution to the northeast Pacific: seasonal variations and transport pathways of carbon monoxide. J. Geophys. Res. 109, D23S07 https://doi.org/10.1029/2003id004402.
- Lin, Y., Fan, J., Li, P., Leung, L.-Y.R., Demott, P.J., Goldberger, L., et al., 2022a. Modeling impacts of ice-nucleating particles from marine aerosols on mixed-phase orographic clouds during 2015 ACAPEX field campaign. Atmos. Chem. Phys. 22, 6749–6771. https://doi.org/10.5194/acp-22-6749-2022.
- Lin, Y., Wang, Y., Pan, B., Hu, J., Guo, S., Levy Zamora, M., et al., 2022b. Formation, radiative forcing, and climatic effects of severe regional haze. Atmos. Chem. Phys. 22, 4951–4967. https://doi.org/10.5194/acp-22-4951-2022.
- Liu, T., Liu, Q., Chen, Y., Wang, W., Zhang, H., Li, D., et al., 2020. Effect of aerosols on the macro- and micro-physical properties of warm clouds in the Beijing-Tianjin-Hebei region. Sci. Total Environ. 720, 137618 https://doi.org/10.1016/j. scitotenv.2020.137618.
- Liu, Q., Duan, S., He, Q., Chen, Y., Zhang, H., Cheng, N., et al., 2021. The variability of warm cloud droplet radius induced by aerosols and water vapor in Shanghai from MODIS observations. Atmos. Res. 253, 105470 https://doi.org/10.1016/j. atmosres.2021.105470.
- Logan, T., Xi, B., Dong, X., 2014. Aerosol properties and their influences on marine boundary layer cloud condensation nuclei at the ARM mobile facility over the Azores. J. Geophys. Res. 119, 4859–4872. https://doi.org/10.1002/2013jd021288.
- Logan, T., Dong, X., Xi, B., 2018. Aerosol properties and their impacts on surface CCN at the ARM southern Great Plains site during the 2011 Midlatitude continental convective clouds experiment. Adv. Atmos. Sci. 35, 224–233. https://doi.org/ 10.1007/s00376-017-7033-2.
- Lu, Z., Liu, X., Zhang, Z., Zhao, C., Meyer, K., Rajapakshe, C., et al., 2018. Biomass smoke from southern Africa can significantly enhance the brightness of stratocumulus over the southeastern Atlantic Ocean. Proc. Natl. Acad. Sci. U. S. A. 115, 2924–2929. https://doi.org/10.1073/pnas.1713703115.
- Maring, H., 2003. Vertical distributions of dust and sea-salt aerosols over Puerto Rico during PRIDE measured from a light aircraft. J. Geophys. Res. 108 (D19), 8587. https://doi.org/10.1029/2002id002544.
- Mather, J.H., Voyles, J.W., 2013. The ARM climate research facility: a review of structure and capabilities. Bull. Am. Meteorol. Soc. 94, 377–392. https://doi.org/10.1175/ Bams-D-11-00218.1.
- Mauger, G.S., Norris, J.R., 2007. Meteorological bias in satellite estimates of aerosol-cloud relationships. Geophys. Res. Lett. 34, L16824 https://doi.org/10.1029/2007gl029952.
- Mcfarquhar, G.M., Wang, H., 2006. Effects of aerosols on trade wind cumuli over the Indian Ocean: model simulations. Q. J. R. Meteorol. Soc. 132, 821–843. https://doi. org/10.1256/qi.04.179.
- Meloni, D., di Sarra, A., Di Iorio, T., Fiocco, G., 2005. Influence of the vertical profile of Saharan dust on the visible direct radiative forcing. J. Quant. Spectrosc. Radiat. Transf. 93, 397–413. https://doi.org/10.1016/j.jqsrt.2004.08.035.
 Minguillón, M.C., Brines, M., Pérez, N., Reche, C., Pandolfi, M., Fonseca, A.S., et al.,
- Minguillon, M.C., Brines, M., Perez, N., Reche, C., Pandolfi, M., Fonseca, A.S., et al., 2015. New particle formation at ground level and in the vertical column over the Barcelona area. Atmos. Res. 164-165, 118–130. https://doi.org/10.1016/j. atmosres.2015.05.003.
- Myhre, G., Shindell, D., 2013. Anthropogenic and natural radiative forcing. In: Stocker, T.F. (Ed.), Climate Change 2013: The Physical Science Basis. Cambridge University Press. Cambridge.
- Osborne, S.R., Haywood, J.M., 2005. Aircraft observations of the microphysical and optical properties of major aerosol species. Atmos. Res. 73, 173–201. https://doi. org/10.1016/j.atmosres.2004.09.002.
- Painemal, D., Kato, S., Minnis, P., 2014. Boundary layer regulation in the southeast Atlantic cloud microphysics during the biomass burning season as seen by the Atrain satellite constellation. J. Geophys. Res. 119, 11,288–11,302. https://doi.org/ 10.1002/2014JD022182.
- Peters, K., Quaas, J., Bellouin, N., 2011. Effects of absorbing aerosols in cloudy skies: a satellite study over the Atlantic Ocean. Atmos. Chem. Phys. 11, 1393–1404. https://doi.org/10.5194/acp-11-1393-2011.
- Raes, F., Liao, H., Chen, W.-T., Seinfeld, J.H., 2010. Atmospheric chemistry-climate feedbacks. J. Geophys. Res. 115, D12121 https://doi.org/10.1029/2009jd013300.
- Ramanathan, V., Crutzen, P.J., Kiehl, J.T., Rosenfeld, D., 2001. Aerosols, climate, and the hydrological cycle. Science 294, 2119–2124. https://doi.org/10.1126/ science 1064034
- Ramanathan, V., Ramana, M.V., Roberts, G., Kim, D., Corrigan, C., Chung, C., et al., 2007. Warming trends in Asia amplified by brown cloud solar absorption. Nature 448, 575–U5. https://doi.org/10.1038/nature06019.
- Rémillard, J., Kollias, P., Luke, E., Wood, R., 2012. Marine boundary layer cloud observations in the Azores. J. Clim. 25, 7381–7398. https://doi.org/10.1175/jcli-d-11-00610.1.
- Rosenfeld, D., Andreae, M.O., Asmi, A., Chin, M., De Leeuw, G., Donovan, D.P., et al., 2014. Global observations of aerosol-cloud-precipitation-climate interactions. Rev. Geophys. 52, 750–808. https://doi.org/10.1002/2013RG000441.
- Russell, P.B., Hobbs, P.V., Stowe, L.L., 1999. Aerosol properties and radiative effects in the United States East Coast haze plume: an overview of the tropospheric aerosol radiative forcing observational experiment (TARFOX). J. Geophys. Res. 104, 2213–2222. https://doi.org/10.1029/1998jd200028.
- Schmid, B., Ferrare, R., Flynn, C., Elleman, R., Covert, D., Strawa, A., et al., 2006. How well do state-of-the-art techniques measuring the vertical profile of tropospheric

- aerosol extinction compare? J. Geophys. Res. 111, D05S07 https://doi.org/10.1029/
- Schmid, B., Flynn, C.J., Newsom, R.K., Turner, D.D., Ferrare, R.A., Clayton, M.F., et al., 2009. Validation of aerosol extinction and water vapor profiles from routine atmospheric radiation measurement program climate research facility measurements. J. Geophys. Res. 114, D22207 https://doi.org/10.1029/ 2009jd012682.
- Sun, Y., Zhao, C., 2020. Influence of Saharan dust on the large-scale meteorological environment for development of tropical cyclone over North Atlantic Ocean basin. J. Geophys. Res. 125, e2020JD033454 https://doi.org/10.1029/2020JD033454.
- Sun, Y., Zhao, C., 2021. Distinct impacts on precipitation by aerosol radiative effect over three different megacity regions of eastern China. Atmos. Chem. Phys. 21, 16555–16574. https://doi.org/10.5194/acp-21-16555-2021.
- Tao, W.K., Chen, J.P., Li, Z.Q., Wang, C., Zhang, C.D., 2012. Impact of aerosols on convective clouds and precipitation. Rev. Geophys. 50, RG2001 https://doi.org/ 10.1029/2011re000369
- Thorsen, T.J., Fu, Q., 2015. Automated retrieval of cloud and aerosol properties from the ARM Raman Lidar. Part II: extinction. J. Atmos. Ocean. Technol. 32, 1999–2023. https://doi.org/10.1175/ltech-D-14-00178.1.
- Thorsen, T.J., Fu, Q., Newsom, R.K., Turner, D.D., Comstock, J.M., 2015. Automated retrieval of cloud and aerosol properties from the ARM Raman Lidar. Part I: feature detection. J. Atmos. Ocean. Technol. 32, 1977–1998. https://doi.org/10.1175/ Jtech-D-14-00150.1.
- Thorsen, T.J., Ferrare, R.A., Hostetler, C.A., Vaughan, M.A., Fu, Q., 2017. The impact of lidar detection sensitivity on assessing aerosol direct radiative effects. Geophys. Res. Lett. 44, 9059–9067. https://doi.org/10.1002/2017gl074521.
- Turner, D.D., Clough, S.A., Liljegren, J.C., Clothiaux, E.E., Cady-Pereira, K.E., Gaustad, K. L., 2007. Retrieving liquid Wat0er path and precipitable water vapor from the atmospheric radiation measurement (ARM) microwave radiometers. IEEE Trans. Geosci. Remote Sens. 45, 3680–3690. https://doi.org/10.1109/TGRS.2007.903703.
- Varble, A., 2018. Erroneous attribution of deep convective invigoration to aerosol concentration. J. Atmos. Sci. 75, 1351–1368. https://doi.org/10.1175/jas-d-17-0217.1
- Wang, Z., Menenti, M., 2021. Challenges and opportunities in Lidar remote sensing. Front. Remote Sens. 2 https://doi.org/10.3389/frsen.2021.641723.
- Wang, Y., Khalizov, A., Levy, M., Zhang, R.Y., 2013. New directions: light absorbing aerosols and their atmospheric impacts. Atmos. Environ. 81, 713–715. https://doi. org/10.1016/j.atmoseny.2013.09.034.
- Wang, Y., Vogel, J.M., Lin, Y., Pan, B., Hu, J., Liu, Y., et al., 2018. Aerosol microphysical and radiative effects on continental cloud ensembles. Adv. Atmos. Sci. 35, 234–247. https://doi.org/10.1007/s00376-017-7091-5.
- Wang, Y., Zheng, X., Dong, X., Xi, B., Wu, P., Logan, T., et al., 2020. Impacts of long-range transport of aerosols on marine-boundary-layer clouds in the eastern North Atlantic. Atmos. Chem. Phys. 20, 14741–14755. https://doi.org/10.5194/acp-20-14741-2020.
- Whiteaker, J.R., Suess, D.T., Prather, K.A., 2002. Effects of meteorological conditions on aerosol composition and mixing state in Bakersfield, CA. Environ. Sci. Technol. 36, 2345–2353. https://doi.org/10.1021/es011381z.
- Winker, D.M., Vaughan, M.A., Omar, A., Hu, Y., Powell, K.A., Liu, Z., et al., 2009. Overview of the CALIPSO Mission and CALIOP data processing algorithms. J. Atmos. Ocean. Technol. 26, 2310–2323. https://doi.org/10.1175/2009jtecha1281.1.

- Won, J.-G., Yoon, S.-C., Kim, S.-W., Jefferson, A., Dutton, E.G., Holben, B.N., 2004. Estimation of direct radiative forcing of Asian dust aerosols with Sun/sky radiometer and Lidar measurements at Gosan, Korea. J. Meteorol. Soc. Jpn. Ser. II 82, 115–130. https://doi.org/10.2151/jmsj.82.115.
- Wood, R., Wyant, M., Bretherton, C.S., Rémillard, J., Kollias, P., Fletcher, J., et al., 2015. Clouds, aerosols, and precipitation in the marine boundary layer: an arm mobile facility deployment. Bull. Am. Meteorol. Soc. 96, 419–440. https://doi.org/10.1175/ hams-d.13.00180.1
- Wu, Y., de Graaf, M., Menenti, M., 2017. The impact of aerosol vertical distribution on aerosol optical depth retrieval using CALIPSO and MODIS data: case study over dust and smoke regions. J. Geophys. Res. 122, 8801–8815. https://doi.org/10.1002/ 2016.ID026355
- Yang, Y., Zhao, C., Wang, Y., Zhao, X., Sun, W., Yang, J., Ma, Z., Fan, H., 2021. Multi-source data based investigation of aerosol-cloud interaction over the North China plain and North of the Yangtze plain. J. Geophys. Res. 126, e2021JD035609 https://doi.org/10.1029/2021jd035609.
- Yuan, T., Li, Z., Zhang, R., Fan, J., 2008. Increase of cloud droplet size with aerosol optical depth: an observation and modeling study. J. Geophys. Res. 113, D04201. https://doi.org/10.1029/2007JD008632.
- Zarzycki, C.M., Bond, T.C., 2010. How much can the vertical distribution of black carbon affect its global direct radiative forcing? Geophys. Res. Lett. 37, L20807. https://doi. org/10.1029/2010gl044555.
- Zhang, L., Li, Q.B., Gu, Y., Liou, K.N., Meland, B., 2013. Dust vertical profile impact on global radiative forcing estimation using a coupled chemical-transport-radiativetransfer model. Atmos. Chem. Phys. 13, 7097–7114. https://doi.org/10.5194/acp-13-7097-2013.
- Zhang, M., Deng, X., Zhu, R., Ren, Y., Xue, H., 2021. The impact of aerosol vertical distribution on a deep convective cloud. Atmosphere-Basel 12, 675. https://doi.org/ 10.3390/atmos12060675
- Zhao, T.L., Gong, S.L., Huang, P., Lavoué, D., 2012. Hemispheric transport and influence of meteorology on global aerosol climatology. Atmos. Chem. Phys. 12, 7609–7624. https://doi.org/10.5194/acp-12-7609-2012.
- Zhao, B., Liou, K.N., Gu, Y., Jiang, J.H., Li, Q., Fu, R., et al., 2018a. Impact of aerosols on ice crystal size. Atmos. Chem. Phys. 18, 1065–1078. https://doi.org/10.5194/acp-18.1065-2018
- Zhao, B., Jiang, J.H., Diner, D.J., Su, H., Gu, Y., Liou, K.N., et al., 2018b. Intra-annual variations of regional aerosol optical depth, vertical distribution, and particle types from multiple satellite and ground-based observational datasets. Atmos. Chem. Phys. 18, 11247–11260. https://doi.org/10.5194/acp-18-11247-2018.
- Zhao, B., Wang, Y., Gu, Y., Liou, K.N., Jiang, J.H., Fan, J., et al., 2019. Ice nucleation by aerosols from anthropogenic pollution. Nat. Geosci. 12, 602–607. https://doi.org/ 10.1038/s41561-019-0389-4.
- Zhao, X., Zhao, C., Yang, Y., Sun, Y., Xia, Y., 2022. Dust aerosol impacts on the time of cloud formation in the Badain Jaran Desert area. J. Geophys. Res. 127, e2022JD037019 https://doi.org/10.1029/2022JD037019.
- Zheng, X., Xi, B., Dong, X., Logan, T., Wang, Y., Wu, P., 2020. Investigation of aerosol-cloud interactions under different absorptive aerosol regimes using atmospheric radiation measurement (ARM) southern Great Plains (SGP) ground-based measurements. Atmos. Chem. Phys. 20, 3483–3501. https://doi.org/10.5194/acp-20-3483-2020.